

# One-dimensional $\mathbb{Z}$ -classified topological crystalline insulator under space-time inversion symmetry

Ling Lin<sup>1,2,\*</sup>, Yongguan Ke<sup>1,2,†</sup> and Chaohong Lee<sup>1,2,‡</sup>

<sup>1</sup>*Institute of Quantum Precision Measurement, State Key Laboratory of Radio Frequency Heterogeneous Integration, College of Physics and Optoelectronic Engineering, Shenzhen University, Shenzhen 518060, China and*

<sup>2</sup>*Quantum Science Center of Guangdong-Hong Kong-Macao Greater Bay Area (Guangdong), Shenzhen 518045, China*

(Dated: November 4, 2024)

We explore a large family of one-dimensional (1D) topological crystalline insulators (TCIs) classified by  $\mathbb{Z}$  invariants under space-time inversion symmetry. This finding stands in marked contrast to the conventional classification of 1D band topology protected by inversion symmetry and characterized by  $\mathbb{Z}_2$ -quantized polarization (Berry-Zak phase). By considering the nontrivial relative polarization among sublattices (orbitals), we introduce the inversion winding number as a topological invariant for characterizing and categorizing band topology. The inversion winding number reliably captures a novel bulk-edge correspondence, where gapped edge states are related to the inversion winding number of the sandwiching bands. Leveraging real-space analysis, we discover disorder-induced topological Anderson insulators and propose to experimentally discern band topology through relative polarization of edge states or bulk states. Our comprehensive findings present a paradigmatic illustration for the ongoing investigation and classification of band topology in TCIs.

*Introduction.* Crystalline symmetry plays an important role in classifying topological insulators [1–6], complementary to the three intrinsic symmetries (i.e. chiral, time-reversal, and particle-hole symmetries). Tremendous topological states protected by crystalline symmetries, known as topological crystalline insulators (TCIs), have been explored [1–7]. In recent years, systematic search for TCIs has been achieved by analyzing high-symmetry points in momentum space and chemical orbitals in real space [2, 3]. TCIs exhibit nontrivial topological properties such as corner states [8, 9], quantized multipole moments [9, 10], non-Abelian topological charges [6, 11–13], and period-multiplied Bloch oscillations [14, 15]. These properties show that crystalline symmetries introduce richer topological structures, and may have promising applications in spintronics, quantum computing, and novel electronic devices.

In one dimension (1D), the inversion symmetry is essential for realizing TCI [16–21]. Given a gapped band, the polarization  $p$  related to the Berry-Zak phase is widely used as a  $\mathbb{Z}_2$ -quantized invariant to characterize different 1D TCIs [20, 22–26], though it may fail to predict the bulk-edge correspondence [27]. For composite multiple bands, one can utilize the inversion eigenvalues at high-symmetry points or the Wilson loop to identify a non-negative integer invariant  $\mathbb{Z}^{\geq}$  [10, 16, 17, 28]. In the presence of chiral symmetry, it is well known that the band topology in 1D transcends  $\mathbb{Z}_2$  classification and falls into the  $\mathbb{Z}$  classification, which can be characterized by the chiral winding number [29, 30]. Notably, it has been discovered that the chiral winding number can be equivalently expressed as the polarization difference between the two sublattices (or orbitals) [31–33], offering a more fundamentally physical perspective on comprehending 1D chiral-symmetric topological insulators. The

number of in-gap zero modes is proportional to the chiral winding number, meaning that nontrivial relative polarization between sublattices can give rise to nontrivial boundary states. Therefore, in the absence of chiral symmetry, a natural question arises: *Can nontrivial relative inter-sublattice polarization exist as a result of crystalline symmetry and further categorize the band topology in 1D?*

In this Letter, we present a theory demonstrating that, under space-time inversion symmetry, exotic topological structures can exist in a large family of 1D TCIs. Space-time inversion symmetry, referring to the combination of inversion symmetry and time-reversal symmetry, is expressed by

$$\mathcal{I}\mathcal{T}H(k)(\mathcal{I}\mathcal{T})^{-1} = H(k), \quad (1)$$

where  $k$  is the quasi momentum,  $\mathcal{I}$  denotes the space-inversion operator and  $\mathcal{T}$  represents the time-reversal operator. The space-time inversion symmetry imposes constraints on the Bloch Hamiltonian and its eigenvectors locally within the momentum space. This phenomenon brings internal topological structures to the Bloch states, enabling a substantial classification of band topology within 1D TCIs. Our work gives insights into systematic exploration of TCIs with hidden topological structures in higher dimensions.

*Three-band model and inversion winding number.* We consider a simple but general three-band model with space-time inversion symmetry (1). Its Hamiltonian matrix and inversion operator are given by

$$H(k) = \begin{pmatrix} \Delta_k & g_k & h_k \\ g_k^* & -\Delta_k & g_k \\ h_k^* & g_k^* & \Delta_k \end{pmatrix}, \quad \mathcal{I} = \begin{pmatrix} 0 & 0 & 1 \\ 0 & 1 & 0 \\ 1 & 0 & 0 \end{pmatrix}, \quad (2)$$

with  $g_k, h_k \in \mathbb{C}$  being complex parameters and  $\Delta_k \in \mathbb{R}$  being real parameter. The time-reversal operation on the

Bloch Hamiltonian here is the complex conjugation operation:  $\mathcal{T}H(k)\mathcal{T}^{-1} = H(k)^*$ . Clearly, this model has no chiral symmetry. Due to the space-time inversion symmetry, the eigenvector of  $H(k)$  can be written as a general form

$$\mathbf{u}_k = \left( \alpha_k e^{-i\xi_k} \quad \beta_k e^{-i\frac{\xi_k}{2}} \quad \alpha_k^* \right)^T \quad (3)$$

with  $\xi_k \in [0, 2\pi)$ ,  $\alpha_k \in \mathbb{C}$  and  $\beta_k \in \mathbb{R}$ . For simplicity, we have omitted the band index and assumed that all bands are gapped. Under the inversion transformation, we have  $(\mathcal{I}\mathbf{u}_k)^* = e^{i\xi_k}\mathbf{u}_k$ . In particular, the first and third sublattices are related by a space-time inversion operation, and the phase factor associated with  $\xi_k$  cannot be gauged out. This leads to the possible presence of nontrivial topological structures among the sublattices.

It is important to note that, in 1D chiral-symmetric topological insulators, the polarization difference between two sublattices can lead to nontrivial polarizations and charge accumulations at the edge [31, 33, 34]. This phenomenon is associated with the chiral winding number belonging to the  $\mathbb{Z}$  class. Thus, in the 1D TCIs with space-time inversion symmetry, we define a gauge-invariant winding number via the sublattice polarization difference between the first and the third sublattice,

$$\nu = \frac{1}{\pi i} \int_0^{2\pi} dk \left[ \frac{\langle u_k | \frac{\partial}{\partial k} (\hat{P}_3 - \hat{P}_1) | u_k \rangle}{\langle u_k | \hat{P}_1 + \hat{P}_3 | u_k \rangle} \right], \quad (4)$$

where  $\hat{P}_\sigma = \sum_k |k, \sigma\rangle\langle k, \sigma|$  is the projector onto the  $\sigma = 1, 2, 3$  sublattice with  $|k, \sigma\rangle$  being the basis of the momentum space, and  $\langle u_k | \hat{P}_1 + \hat{P}_3 | u_k \rangle$  denotes the normalization factor. Due to the inversion symmetry, one can find  $\langle u_k | \hat{P}_1 | u_k \rangle = \langle u_k | \hat{P}_3 | u_k \rangle$ . This gauge-invariant quantity is quantized to integers  $\nu \in \mathbb{Z}$  and it is directly related to the quantized polarization such that  $p = \nu/2 \pmod{1}$  [35]. It is worth noting that the inversion winding number shares some similarities with the mirror Chern number, where the difference of the Chern number between the two sectors having different mirror eigenvalues constitutes the mirror Chern number [36, 37]. In our study, the inversion winding number is obtained via projection onto the two inversion-symmetric sublattices.

Below we discuss the topological stability of the defined inversion winding number (4). It can be found that the inversion winding number becomes ill-defined when  $\alpha_k = 0$  in Eq. (3). To change the value of the inversion winding number, the system must pass this singular point. To find in what condition that  $\alpha_k = 0$ , we solve the eigenvalue equation  $H(k)u_k = E_k u_k$  by assuming  $\alpha_k = 0$ . We find that  $g_k = 0$  is necessary for  $\alpha_k = 0$ . It can be concluded that, to change the inversion winding number, one must either break the space-time inversion symmetry, close the spectral gap, or introduce certain terms to ensure that  $g_k = 0$ . Generally speaking, the

topological protection in TCIs manifests that the target system cannot be adiabatically connected to other distinct TCI phases without closing the spectral gap and breaking the underlying symmetry. In this sense, the inversion winding number here seems unstable, as it may possibly change through tuning  $g_k = 0$ . Nevertheless, the inversion winding number is related to the polarization via  $p = \nu/2 \pmod{1}$ . Strictly speaking, the parity of the inversion winding number is a  $\mathbb{Z}_2$  topological invariant. Although the inversion winding number becomes ill-defined when  $\alpha_k = 0$ , it is still possible to introduce perturbations to ensure that  $g_k \neq 0$ , thereby avoiding this singular point.

Fortunately, the condition  $g_k \neq 0$  for avoiding the singular point naturally arises in most realistic systems. As the parameter  $g_k \propto \sum_{j \leq j'} t_{j,j'}^{\sigma,\sigma'} e^{ik(j-j')}$  describes the coupling strength between  $\sigma = \{1, 3\}$  and  $\sigma' = 2$  sublattices in momentum space, one can find that  $g_k = 0$  physically requires some very special tunneling terms in real space. Here,  $t_{j,j'}^{\sigma,\sigma'}$  represents the tunneling strength from the  $\sigma$  sublattice in the  $j$ th cell to the  $\sigma'$  sublattice in the  $j'$ th cell in real space. For example, if we set  $g_k = 0$  for all  $k \in \text{B.Z.}$ , some certain lattices become completely isolated, resulting in the system being in the atomic limit. Therefore, we can assert that by excluding those specific conditions to ensure that  $g_k \neq 0$ , the inversion winding number remains topologically stable. This argument remains valid for a large family of systems, offering a more comprehensive classification for space-time inversion-invariant systems. Later, we will provide some evidence to support this point.

*Prototypical model and bulk-edge correspondence.* To show the validity of the defined inversion winding number and demonstrate its  $\mathbb{Z}$  classification, we choose  $g_k = -t_1$ ,  $h_k = -t_2 e^{-ik} - \eta e^{-2ik}$  and  $\Delta_k = 0$ , which corresponds to a system with long-range tunneling in real space. The real-space formulation of this model can be found in Supplementary Material. By varying  $\eta/t_1$ , the spectrum under open boundary condition (OBC) is shown in Fig. 1 (a), comprising three bands labeled as  $n = 1, 2, 3$  from the bottom to the top. In both the first and second band gaps, several in-gap states appear. These in-gap states correspond to edge states that are exponentially localized near the two boundaries. To better elucidate the results, we concentrate on the lowest gap and designate four regions (i-iv) separated by gap-closing points and delve into its topological properties. Intriguingly, there are three different phases. We find that the in-gap edge states exhibit a four-fold degeneracy in regions (i) and (iv), and a two-fold degeneracy in region (ii). In region (iii), there is no in-gap edge state. This suggests that these three regions are three distinct phases.

Subsequently, we calculate the inversion winding number (4) under the periodic boundary condition (PBC), see Figs. 1 (b1-b3). Remarkably, the inversion winding

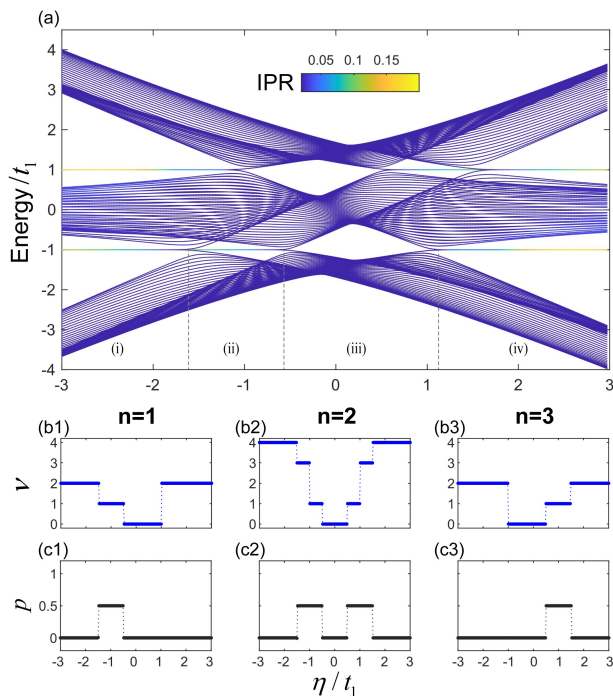


FIG. 1. (a) Energy spectrum under the OBC as a function of  $\eta/t_1$ . The color of each line corresponds to the inverse participation ratio of the eigenstate:  $\text{IPR} = \sum_{j,\sigma} |\langle \psi_n | j, \sigma \rangle|^4$ , which reflects the localization property of an eigenstate. Grey-dashed lines roughly indicate the gap-closing point between the first and second bands and divide into four regions (i-iv). (b1-b3) Inversion winding number for the three bands ( $n = 1, 2, 3$ ) as functions of  $\eta/t_1$  under PBC. (c1-c3) Polarization of the three bands under PBC. Other parameters are chosen as  $t_2/t_1 = 1/2$ .

number identifies more distinct phases and its variation coincides with the locations of gap-closing points. Under the OBC, the number of edge states closely relates to the inversion winding number of the adjacent bands. For instance, the numbers of in-gap edge states in the first and second gaps are respectively proportional to the inversion winding numbers of the first ( $n = 1$ ) and third ( $n = 3$ ) bands:  $N_{\text{edge}}^{\#1} = 2|\nu_1|$  and  $N_{\text{edge}}^{\#2} = 2|\nu_3|$ , where  $N_{\text{edge}}^{\#m}$  and  $\nu_n$  respectively denote the number of edge states in the  $m$ th gap and the inversion winding number of the  $n$ th band. Regarding the second band ( $n = 2$ ), its inversion winding number is the sum of the first and third bands:  $\nu_2 = \nu_1 + \nu_3$ , and the change of this inversion winding number requires the closing of either the first or the second band gap. It can be further deduced that the nontrivial topology of the second band contributes to the emergence of in-gap edge states in both band gaps.

To elucidate the bulk-edge correspondence more profoundly, we consider a continuous connection between the PBC and the OBC. This transition can be effectively modeled by introducing a real-valued parameter  $r \in [0, 1]$  to the tunneling:  $t_{j,j'}^{\sigma,\sigma'} \rightarrow r t_{j,j'}^{\sigma,\sigma'}$  when  $j, j'$

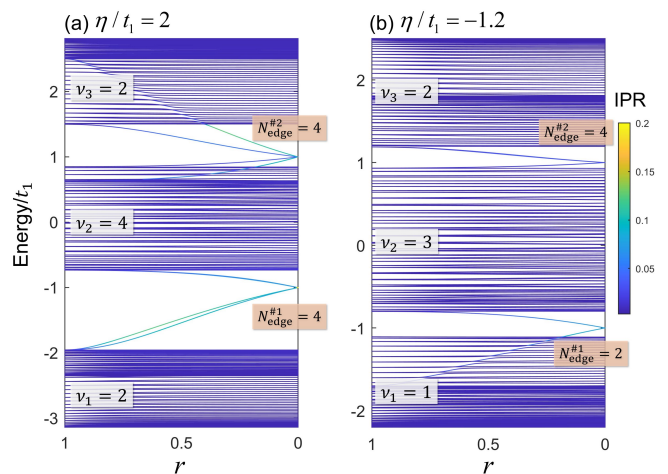


FIG. 2. Energy spectrum versus the real-valued parameter  $r \in [0, 1]$ . Here,  $r = 1$  corresponds to the PBC, while  $r = 0$  corresponds to the OBC. The inversion winding number ( $\nu_n$ ) of each band ( $n = 1, 2, 3$ ) under PBC and the number of edge states ( $N_{\text{edge}}^{\#m}$ ) in each gap ( $m = 1, 2$ ) under OBC are explicitly labelled accordingly, which clearly manifests the bulk-edge correspondence.

crosses the boundary under PBC. Thereby,  $r = 1$  corresponds to the PBC, while  $r = 0$  corresponds to the OBC, which allows the emergency of edge states. As depicted in Fig. 2 (a-b), edge states arise from the two adjacent bands, with their number related to the inversion winding number. The number of edge states arising from the second band is equal to the number of edge states arising from the other two bands. These findings not only reveal a more extensive classification of the band topology protected by the space-time inversion symmetry, but also well demonstrate the nature of bulk-edge correspondence for the inversion winding number. More discussions about the bulk-edge correspondence can be found in the Supplementary Material [35].

For comparison, we calculate the polarization for each band, as shown in Figs. 1 (c1-c3). Generally, the emergence of in-gap edge states is expected as a result of non-zero band polarization, which can be calculated using the Berry-phase formalism under PBC [38, 39]:  $p_n = 1/2\pi \int_{\text{B.Z.}} dk \langle u_k^n | i \partial u_k^n \rangle \text{ mod } 1$ , with  $n$  being the band index. The polarization provides insights into the center of Wannier function within a unit cell [40]. Owing to the space-time inversion symmetry, the polarization for each gapped band is quantized to either  $p_n = 0$  or  $p_n = 1/2$  [41], which has been widely employed to distinguish the band topology. However, as shown by the numerical results, the polarization is unable to explain the presence of the four-fold degenerate edge states observed above. Therefore, unlike the defined inversion winding number, the polarization fails to identify the rich band topology.

*Robustness of inversion winding number.* Having established the momentum-space formula of inversion

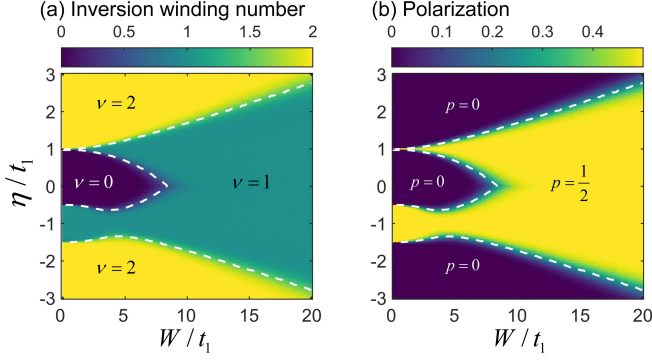


FIG. 3. Phase diagram of the lowest band in the presence of disorder: (a) the inversion winding number and (b) the polarization. Dashed lines indicate the phase boundary determined by the half-height between two phases. Number of cells is  $L = 200$  and other parameters are the same as Fig. 1. All results are averaged over  $10^3$  random realizations.

winding number, we then delve into exploring its real-space counterpart to assess the robustness of band topology against disorder that preserves the space-time inversion symmetry. In analogy to the chiral-symmetric system [33, 42], the real-space formula of the inversion winding number can be expressed as a Bott index form,

$$\nu = -\frac{1}{2\pi} \text{Im} \left\{ \text{Tr} \left[ \log \left( \mathcal{X}_1^\dagger \mathcal{X}_3 \right) \right] \right\}, \quad (5)$$

in which  $\mathcal{X}_\sigma = \Psi^\dagger \exp(i\frac{2\pi}{L}\hat{x}) \hat{P}_\sigma \Psi$  is the projected-position matrix of the  $\sigma = 1, 3$  sublattices and  $\Psi = (\dots, |\psi_j\rangle, \dots)$  denotes a set of eigenstates on the target band. Eq. (5) is equivalent to the momentum-space formula in the presence of translation symmetry [35].

The real-space formula enables us to efficiently calculate the inversion winding number in the presence of inversion-invariant disorder. Here, we introduce disorders to the nearest-neighbor tunneling between the first and third sublattice:  $\hat{H}_{dis} = -W \sum_j \delta_x |x, 1\rangle \langle x, 3| + \text{H.c.}$ , wherein  $\delta_x \in [-1/2, 1/2]$  represents a uniformly distributed random variable and  $W$  is the strength of disorder. Here,  $|x, \sigma\rangle$ ,  $x = 1, 2, \dots, L$  denotes the position basis. To preserve the space-time inversion symmetry, we enforce  $\hat{I} \hat{H}_{dis} \hat{I}^{-1} = (\hat{H}_{dis})^*$ . Meanwhile, this term only entails the coupling between the sublattices  $\sigma = 1$  and  $\sigma = 3$ . As mentioned earlier, the inversion winding number retains its well-defined nature as long as  $t_1 \neq 0$  in this system.

Subsequently, by utilizing Eq. (5), we calculate the  $\eta$ - $W$  phase diagram of inversion winding number for the lowest band under PBC, see Fig. 3 (a). Remarkably, the real-space formula yields a quantized value in every random realization. For weak disorder strength ( $W/t_1 \ll 1$ ), the first band gap remains finite and the fluctuations of the inversion winding number are nearly zero, as shown in Figs. 3 (c) and (d). As the disorder strength inten-

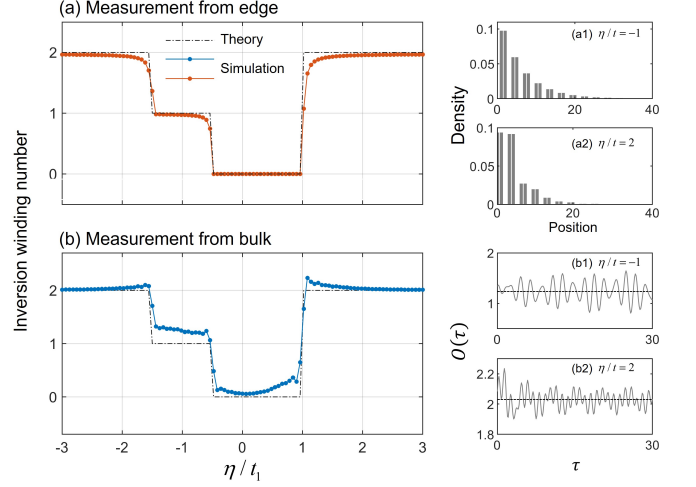


FIG. 4. Simulation of experimentally measuring the inversion winding number. (a) Measuring through the density distribution of edge states in the first gap. (a1-a2) shows two examples of the edge states (only the left end is shown for simplicity). (b) Measuring through the time-evolution method with the total evolution time being  $T = 30/t_1$ . The system's size is chosen as  $L = 200$ . Other parameters are the same as Fig. 1.

sifies, we observe the emergence of a disorder-induced topological transition. Particularly, there is the disorder-induced topological phase ( $\nu = 0 \rightarrow \nu = 1$ ), which is identified as the topological Anderson insulating phase [32, 43–48]. Significant statistical fluctuations in the inversion winding number are observed around all phase transitions. Away from the phase transition points, the inversion winding number remains remarkably stable in broad areas for different random realizations. More detailed discussions, including the evidence for bulk-edge correspondence, can be found in the Supplementary Material [35].

For comparison, we calculate the polarization through the projected position operator methods [10, 49, 50], as shown in Fig. 3 (b). Due to the inversion symmetry, the polarization is also quantized. The polarization  $p$  is connected to the inversion winding number  $\nu$  through the relation  $p = \nu/2 \pmod{1}$ . As expected, the polarization fails to distinguish the phase of  $\nu = 0$  and 2.

*Real-space characterization of band topology.* In above, we have found that the inversion winding number is associated with the polarization difference between two sublattices. This offers the feasibility for experimentally characterizing different topological phases. Under the OBC, the inversion winding number can be approximately extracted from bulk states or edge states via

$$\nu = (-1)^x \frac{2}{L} \sum_{n \in \text{target}} \frac{\langle \psi_n | \hat{X}_3 - \hat{X}_1 | \psi_n \rangle}{\langle \psi_n | \hat{P}_3 + \hat{P}_1 | \psi_n \rangle} \quad (6)$$

in which  $\hat{X}_\sigma = \hat{x} \hat{P}_\sigma$  is the position operator projected



to the  $\sigma = \{1, 2, 3\}$  sublattice. Eq. (6) is a summation over bulk states in a certain band ( $\chi = 1$ ) or edge states in a certain gap ( $\chi = 0$ ). It implies that one can measure the inversion winding number through the bulk or the edge states. In experiments, the edge states can be probed via versatile approaches and then the information of inversion winding number can be directly extracted. As for the bulk state, it is also feasible to measure the winding number through time-evolution [32, 51–56]:  $\nu \approx \lim_{T \rightarrow \infty} \frac{1}{T} \int_0^T d\tau O(\tau)$  with  $O(\tau) = \frac{\langle \Psi(\tau) | \hat{X}_3 - \hat{X}_1 | \Psi(\tau) \rangle}{\langle \Psi(\tau) | \hat{P}_3 + \hat{P}_1 | \Psi(\tau) \rangle}$  and  $|\Psi(\tau)\rangle$  being a superposition of bulk states in a certain band. In Fig. 4, we present our numerical simulation for the experimental measurement through edge states or bulk states [35]. Remarkably, both methods produces a very prominent results compared with the theoretical prediction. The tiny difference between them can be attributed to the finite-size effect and the relatively small spectral gap, especially for bulk measurement. This again highlights the bulk-edge correspondence principle in this system: the appearance of in-gap edge state is a result of the nontrivial sublattice polarization of a band. The nontrivial inversion winding number has prominent physical consequences. The above results can be verified in various systems, such as, electrical circuits [57, 58], acoustic systems [59, 60] and other photonic or atomic systems [11, 21, 26, 55, 61–66].

*Summary and discussion.* We uncover that, under the space-time inversion symmetry, the band topology can be further classified beyond the conventional  $\mathbb{Z}_2$  classification in a large family of 1D three-band models. Based upon the sublattice polarization difference from the space-time inversion symmetry, we introduce a gauge-invariant winding number: the inversion winding number. The bulk topology and the bulk-edge correspondence can be well characterized by the inversion winding number  $\nu \in \mathbb{Z}$ . In addition, we give a real-space formula for the inversion winding number. We also find that the inversion winding number remains effective even in the presence of strong symmetry-invariant disorders. With the real-space formula for the inversion winding number, one can experimentally identify distinct topological phases in TCIs.

This work is supported by the National Key Research and Development Program of China (Grant No. 2022YFA1404104), the National Natural Science Foundation of China (Grant No. 12025509, Grant No. 12247134 and Grant No. 12275365), and the Natural Science Foundation of Guangdong Province (Grant No. 2023A1515012099).

---

\* Email: linling@szu.edu.cn

† Email: keyg@szu.edu.cn

‡ Email: chleecn@szu.edu.cn, chleecn@gmail.com

- [1] L. Fu, Topological crystalline insulators, *Phys. Rev. Lett.* **106**, 106802 (2011).
- [2] B. Bradlyn, L. Elcoro, J. Cano, M. G. Vergniory, Z. Wang, C. Felser, M. I. Aroyo, and B. A. Bernevig, Topological quantum chemistry, *Nature* **547**, 298 (2017).
- [3] H. C. Po, A. Vishwanath, and H. Watanabe, Symmetry-based indicators of band topology in the 230 space groups, *Nature Communications* **8**, 50 (2017).
- [4] L. Fu and C. L. Kane, Topological insulators with inversion symmetry, *Phys. Rev. B* **76**, 045302 (2007).
- [5] E. Cornfeld and A. Chapman, Classification of crystalline topological insulators and superconductors with point group symmetries, *Phys. Rev. B* **99**, 075105 (2019).
- [6] Q. Wu, A. A. Soluyanov, and T. Bzdušek, Non-Abelian band topology in noninteracting metals, *Science* **365**, 1273 (2019).
- [7] Y. Ando and L. Fu, Topological crystalline insulators and topological superconductors: From concepts to materials, *Annual Review of Condensed Matter Physics* **6**, 361 (2015).
- [8] F. Liu and K. Wakabayashi, Novel topological phase with a zero berry curvature, *Phys. Rev. Lett.* **118**, 076803 (2017).
- [9] W. A. Benalcazar, B. A. Bernevig, and T. L. Hughes, Quantized electric multipole insulators, *Science* **357**, 61 (2017).
- [10] W. A. Benalcazar, B. A. Bernevig, and T. L. Hughes, Electric multipole moments, topological multipole moment pumping, and chiral hinge states in crystalline insulators, *Phys. Rev. B* **96**, 245115 (2017).
- [11] Q. Guo, T. Jiang, R.-Y. Zhang, L. Zhang, Z.-Q. Zhang, B. Yang, S. Zhang, and C. T. Chan, Experimental observation of non-Abelian topological charges and edge states, *Nature* **594**, 195 (2021).
- [12] T. Li and H. Hu, Floquet non-Abelian topological insulator and multifold bulk-edge correspondence, *Nature Communications* **14**, 6418 (2023).
- [13] Q.-D. Wang, Y.-Q. Zhu, S.-L. Zhu, and Z. Zheng, Synthetic non-Abelian topological charges in ultracold atomic gases, *Phys. Rev. A* **110**, 023321 (2024).
- [14] J. Höller and A. Alexandradinata, Topological bloch oscillations, *Phys. Rev. B* **98**, 024310 (2018).
- [15] M. Di Liberto, N. Goldman, and G. Palumbo, Non-abelian bloch oscillations in higher-order topological insulators, *Nature communications* **11**, 5942 (2020).
- [16] T. L. Hughes, E. Prodan, and B. A. Bernevig, Inversion-symmetric topological insulators, *Phys. Rev. B* **83**, 245132 (2011).
- [17] A. Alexandradinata, X. Dai, and B. A. Bernevig, Wilson-loop characterization of inversion-symmetric topological insulators, *Phys. Rev. B* **89**, 155114 (2014).
- [18] K. Shiozaki and M. Sato, Topology of crystalline insulators and superconductors, *Phys. Rev. B* **90**, 165114 (2014).
- [19] M. Xiao, Z. Q. Zhang, and C. T. Chan, Surface impedance and bulk band geometric phases in one-dimensional systems, *Phys. Rev. X* **4**, 021017 (2014).
- [20] Y. Hwang, J. Ahn, and B.-J. Yang, Fragile topology protected by inversion symmetry: Diagnosis, bulk-boundary correspondence, and wilson loop, *Phys. Rev. B* **100**, 205126 (2019).
- [21] S. Vaidya, A. Ghorashi, T. Christensen, M. C. Rechtsman, and W. A. Benalcazar, Topological phases of photonic crystals under crystalline symmetries, *Phys. Rev.*

- B 108, 085116 (2023).**
- [22] J. Zak, Symmetry specification of bands in solids, *Phys. Rev. Lett.* **45**, 1025 (1980).
- [23] J. Zak, Band representations and symmetry types of bands in solids, *Phys. Rev. B* **23**, 2824 (1981).
- [24] J. Zak, Band center—a conserved quantity in solids, *Phys. Rev. Lett.* **48**, 359 (1982).
- [25] J. Zak, Berry’s phase for energy bands in solids, *Phys. Rev. Lett.* **62**, 2747 (1989).
- [26] B. Song, L. Zhang, C. He, T. F. J. Poon, E. Hagiyevev, S. Zhang, X.-J. Liu, and G.-B. Jo, Observation of symmetry-protected topological band with ultracold fermions, *Science Advances* **4**, eaao4748 (2018).
- [27] J.-W. Rhim, J. H. Bardarson, and R.-J. Slager, Unified bulk-boundary correspondence for band insulators, *Phys. Rev. B* **97**, 115143 (2018).
- [28] R. Takahashi, Y. Tanaka, and S. Murakami, Bulk-edge and bulk-hinge correspondence in inversion-symmetric insulators, *Phys. Rev. Res.* **2**, 013300 (2020).
- [29] C.-K. Chiu, J. C. Y. Teo, A. P. Schnyder, and S. Ryu, Classification of topological quantum matter with symmetries, *Rev. Mod. Phys.* **88**, 035005 (2016).
- [30] S. Ryu, A. P. Schnyder, A. Furusaki, and A. W. W. Ludwig, Topological insulators and superconductors: tenfold way and dimensional hierarchy, *New J. Phys.* **12**, 065010 (2010).
- [31] I. Mondragon-Shem, T. L. Hughes, J. Song, and E. Prodan, Topological Criticality in the Chiral-Symmetric AIII Class at Strong Disorder, *Phys. Rev. Lett.* **113**, 046802 (2014).
- [32] E. J. Meier, F. A. An, A. Dauphin, M. Maffei, P. Massignan, T. L. Hughes, and B. Gadway, Observation of the topological Anderson insulator in disordered atomic wires, *Science* **362**, 929 (2018).
- [33] L. Lin, Y. Ke, and C. Lee, Real-space representation of the winding number for a one-dimensional chiral-symmetric topological insulator, *Phys. Rev. B* **103**, 224208 (2021).
- [34] L. Lin and C. Lee, Probing chiral-symmetric higher-order topological insulators with multipole winding number (2024), [arXiv:2401.03699 \[cond-mat.mes-hall\]](https://arxiv.org/abs/2401.03699).
- [35] See Supplementary Material for details of: (S1) band structure and inversion winding number; (S2) derivation of the real-space formula; (S3) discussions on the bulk-edge correspondence; (S4) the quantization relations of topological invariants; (S5) discussion on the real-space model; (S6) discussion on the two- and four-band systems, which includes Refs. [xxx].
- [36] J. C. Y. Teo, L. Fu, and C. L. Kane, Surface states and topological invariants in three-dimensional topological insulators: Application to  $\text{Bi}_{1-x}\text{Sb}_x$ , *Phys. Rev. B* **78**, 045426 (2008).
- [37] T. H. Hsieh, H. Lin, J. Liu, W. Duan, A. Bansil, and L. Fu, Topological crystalline insulators in the SnTe material class, *Nature Communications* **3**, 982 (2012).
- [38] R. D. King-Smith and D. Vanderbilt, Theory of polarization of crystalline solids, *Phys. Rev. B* **47**, 1651 (1993).
- [39] R. Resta, Macroscopic polarization in crystalline dielectrics: the geometric phase approach, *Rev. Mod. Phys.* **66**, 899 (1994).
- [40] N. Marzari, A. A. Mostofi, J. R. Yates, I. Souza, and D. Vanderbilt, Maximally localized Wannier functions: Theory and applications, *Rev. Mod. Phys.* **84**, 1419 (2012).
- [41] J. Ahn, S. Park, D. Kim, Y. Kim, and B.-J. Yang, Stiefel–whitney classes and topological phases in band theory, *Chinese Physics B* **28**, 117101 (2019).
- [42] W. A. Benalcazar and A. Cerjan, Chiral-symmetric higher-order topological phases of matter, *Phys. Rev. Lett.* **128**, 127601 (2022).
- [43] J. Li, R.-L. Chu, J. K. Jain, and S.-Q. Shen, Topological Anderson Insulator, *Phys. Rev. Lett.* **102**, 136806 (2009).
- [44] A. Altland, D. Bagrets, L. Fritz, A. Kamenev, and H. Schmiedt, Quantum Criticality of Quasi-One-Dimensional Topological Anderson Insulators, *Phys. Rev. Lett.* **112**, 206602 (2014).
- [45] B. Wu, J. Song, J. Zhou, and H. Jiang, Disorder effects in topological states: Brief review of the recent developments\*, *Chinese Physics B* **25**, 117311 (2016).
- [46] Q. Lin, T. Li, L. Xiao, K. Wang, W. Yi, and P. Xue, Observation of non-Hermitian topological Anderson insulator in quantum dynamics, *Nature Communications* **13**, 3229 (2022).
- [47] L.-Z. Tang, S.-N. Liu, G.-Q. Zhang, and D.-W. Zhang, Topological Anderson insulators with different bulk states in quasiperiodic chains, *Phys. Rev. A* **105**, 063327 (2022).
- [48] M. Ren, Y. Yu, B. Wu, X. Qi, Y. Wang, X. Yao, J. Ren, Z. Guo, H. Jiang, H. Chen, X.-J. Liu, Z. Chen, and Y. Sun, Realization of Gapped and Ungapped Photonic Topological Anderson Insulators, *Phys. Rev. Lett.* **132**, 066602 (2024).
- [49] R. Resta, Quantum-mechanical position operator in extended systems, *Phys. Rev. Lett.* **80**, 1800 (1998).
- [50] L. Lin, Y. Ke, and C. Lee, Topological invariants for interacting systems: From twisted boundary conditions to center-of-mass momentum, *Phys. Rev. B* **107**, 125161 (2023).
- [51] F. Cardano, A. D’Errico, A. Dauphin, M. Maffei, B. Piccirillo, C. de Lisio, G. De Filippis, V. Cataudella, E. Santamato, L. Marrucci, *et al.*, Detection of zak phases and topological invariants in a chiral quantum walk of twisted photons, *Nature communications* **8**, 15516 (2017).
- [52] X. Wang, L. Xiao, X. Qiu, K. Wang, W. Yi, and P. Xue, Detecting topological invariants and revealing topological phase transitions in discrete-time photonic quantum walks, *Phys. Rev. A* **98**, 013835 (2018).
- [53] D. Xie, W. Gou, T. Xiao, B. Gadway, and B. Yan, Topological characterizations of an extended su–schrieffer–heeger model, *npj Quantum Information* **5**, 55 (2019).
- [54] Y. Wang, Y.-H. Lu, F. Mei, J. Gao, Z.-M. Li, H. Tang, S.-L. Zhu, S. Jia, and X.-M. Jin, Direct observation of topology from single-photon dynamics, *Phys. Rev. Lett.* **122**, 193903 (2019).
- [55] W. Cai, J. Han, F. Mei, Y. Xu, Y. Ma, X. Li, H. Wang, Y. P. Song, Z.-Y. Xue, Z.-q. Yin, S. Jia, and L. Sun, Observation of topological magnon insulator states in a superconducting circuit, *Phys. Rev. Lett.* **123**, 080501 (2019).
- [56] D. Xie, T.-S. Deng, T. Xiao, W. Gou, T. Chen, W. Yi, and B. Yan, Topological quantum walks in momentum space with a bose-einstein condensate, *Phys. Rev. Lett.* **124**, 050502 (2020).
- [57] N. A. Olekhno, A. D. Rozenblit, V. I. Kachin, A. A. Dmitriev, O. I. Burmistrov, P. S. Seregin, D. V. Zhirihin, and M. A. Gorlach, Experimental realization of topological corner states in long-range-coupled electrical circuits, *Phys. Rev. B* **105**, L081107 (2022).

- [58] Y. Li, J.-H. Zhang, F. Mei, B. Xie, M.-H. Lu, J. Ma, L. Xiao, and S. Jia, Large-chiral-number corner modes in  $\mathbb{Z}$ -class higher-order topoelectrical circuits, *Phys. Rev. Appl.* **20**, 064042 (2023).
- [59] D. Wang, Y. Deng, J. Ji, M. Oudich, W. A. Benalcazar, G. Ma, and Y. Jing, Realization of a  $\mathbb{Z}$ -classified chiral-symmetric higher-order topological insulator in a coupling-inverted acoustic crystal, *Phys. Rev. Lett.* **131**, 157201 (2023).
- [60] Y. Li, H. Qiu, Q. Zhang, and C. Qiu, Acoustic higher-order topological insulators protected by multipole chiral numbers, *Phys. Rev. B* **108**, 205135 (2023).
- [61] A. Poddubny, A. Miroschnichenko, A. Slobozhanyuk, and Y. Kivshar, Topological majorana states in zigzag chains of plasmonic nanoparticles, *ACS Photonics* **1**, 101 (2014).
- [62] D.-W. Zhang, Y.-Q. Zhu, Y. X. Zhao, H. Yan, and S.-L. Zhu, Topological quantum matter with cold atoms, *Advances in Physics* **67**, 253 (2018).
- [63] S. Kruk, A. Poddubny, D. Smirnova, L. Wang, A. Slobozhanyuk, A. Shorokhov, I. Kravchenko, B. Luther-Davies, and Y. Kivshar, Nonlinear light generation in topological nanostructures, *Nature Nanotechnology* **14**, 126 (2019).
- [64] T. Ozawa, H. M. Price, A. Amo, N. Goldman, M. Hafezi, L. Lu, M. C. Rechtsman, D. Schuster, J. Simon, O. Zeitlinger, and I. Carusotto, Topological photonics, *Rev. Mod. Phys.* **91**, 015006 (2019).
- [65] H.-X. Wang, G.-Y. Guo, and J.-H. Jiang, Band topology in classical waves: Wilson-loop approach to topological numbers and fragile topology, *New Journal of Physics* **21**, 093029 (2019).
- [66] Z.-Q. Jiao, S. Longhi, X.-W. Wang, J. Gao, W.-H. Zhou, Y. Wang, Y.-X. Fu, L. Wang, R.-J. Ren, L.-F. Qiao, and X.-M. Jin, Experimentally detecting quantized zak phases without chiral symmetry in photonic lattices, *Phys. Rev. Lett.* **127**, 147401 (2021).

# Supplemental Materials for “One-dimensional $\mathbb{Z}$ -classified topological crystalline insulator under space-time inversion symmetry”

Ling Lin<sup>1,2</sup>, Yongguan Ke<sup>1,2</sup>, and Chaohong Lee<sup>1,2\*</sup>

<sup>1</sup>*Institute of Quantum Precision Measurement,  
State Key Laboratory of Radio Frequency Heterogeneous Integration,  
College of Physics and Optoelectronic Engineering,  
Shenzhen University, Shenzhen 518060, China and*

<sup>2</sup>*Quantum Science Center of Guangdong-Hong Kong-Macao  
Greater Bay Area (Guangdong), Shenzhen 518045, China*

(Dated: November 4, 2024)

## CONTENTS

S1. Band structure and the visualized inversion winding number	2
S2. Real-space formula of the inversion winding number	3
A. Equivalence to the momentum-space formula	3
B. Derivation via the twisted boundary condition	4
C. In views of the Wannier state	7
D. More information on the phase diagram in the presence of disorder	7
S3. Bulk-edge correspondence and the inversion winding number	8
Numerical results	12
S4. Space-time inversion symmetry and quantization of topological invariants	13
A. Quantization of the polarization (Berry-Zak phase)	13
B. Quantization of the inversion winding number and its relation to the polarization	14
S5. Real-space model and experimental realization	15

---

\* Corresponding author. Email: [chleecn@szu.edu.cn](mailto:chleecn@szu.edu.cn), [chleecn@gmail.com](mailto:chleecn@gmail.com)



A. Measurement from the edge states	16
B. Measurement from the bulk states	17
S6. More systems	18
A. Two-band systems	18
B. Four-band systems	18
References	21

## S1. BAND STRUCTURE AND THE VISUALIZED INVERSION WINDING NUMBER

The inversion winding number can be written as the following equivalent form:

$$\nu = \frac{1}{2\pi i} \int_0^{2\pi} dk q(k)^{-1} \partial_k q(k), \quad (\text{S1})$$

where  $q_k = \langle u_k | \mathcal{P}_{1,3} | u_k \rangle \in \mathbb{C}$ ,  $\mathcal{P}_{1,3} = \sum_k |k, 1\rangle \langle k, 3|$ . For comprehension, we present the band structure and visualize the inversion winding number of the lowest band in Fig. S1. The inversion winding number is not normalized here and the curve is plotted according to the trajectory of  $q_k$  as a function of  $k \in [0, 2\pi)$  on the complex plane. Notably, for  $\eta/t_1 = 1$ , the band gap between the first band and the second band is closed and the inversion winding number is ill-defined. It displays the band inversion profile at the phase transition point. At the phase transition point, there appears the band crossing point, where the two Bloch states are degenerate. As mentioned in the main text, the change of inversion winding number requires that  $\alpha_k = 0$  in the Bloch state. This is possible due to the band degeneracy at the phase transition point.

Alternatively, by introducing the following pseudo-spin operators:

$$\sigma_x = \begin{pmatrix} 0 & 0 & 1 \\ 0 & 0 & 0 \\ 1 & 0 & 0 \end{pmatrix}, \quad \sigma_y = \begin{pmatrix} 0 & 0 & -i \\ 0 & 0 & 0 \\ i & 0 & 0 \end{pmatrix}, \quad \sigma_z = \begin{pmatrix} 1 & 0 & 0 \\ 0 & 0 & 0 \\ 0 & 0 & -1 \end{pmatrix}, \quad (\text{S2})$$

we can define the spin polarization  $\langle \sigma_\alpha^k \rangle = \langle u_k | \sigma_\alpha | u_k \rangle$ ,  $\alpha = x, y, z$ . With the space-time symmetry, it can be checked that  $\langle \sigma_z^k \rangle = 0$ , meaning that the spin polarization is restricted on the  $x - y$  plane. In particular, it can be found that

$$q_k = \langle \sigma_x^k \rangle + i \langle \sigma_y^k \rangle. \quad (\text{S3})$$

This allows us to equivalently formulate the inversion winding number through the following formula for a gapped band:

$$\nu = \frac{1}{2\pi i} \int_0^{2\pi} dk \frac{\langle \sigma_x^k \rangle \partial_k \langle \sigma_y^k \rangle - \langle \sigma_y^k \rangle \partial_k \langle \sigma_x^k \rangle}{\langle \sigma_x^k \rangle^2 + \langle \sigma_y^k \rangle^2}. \quad (\text{S4})$$

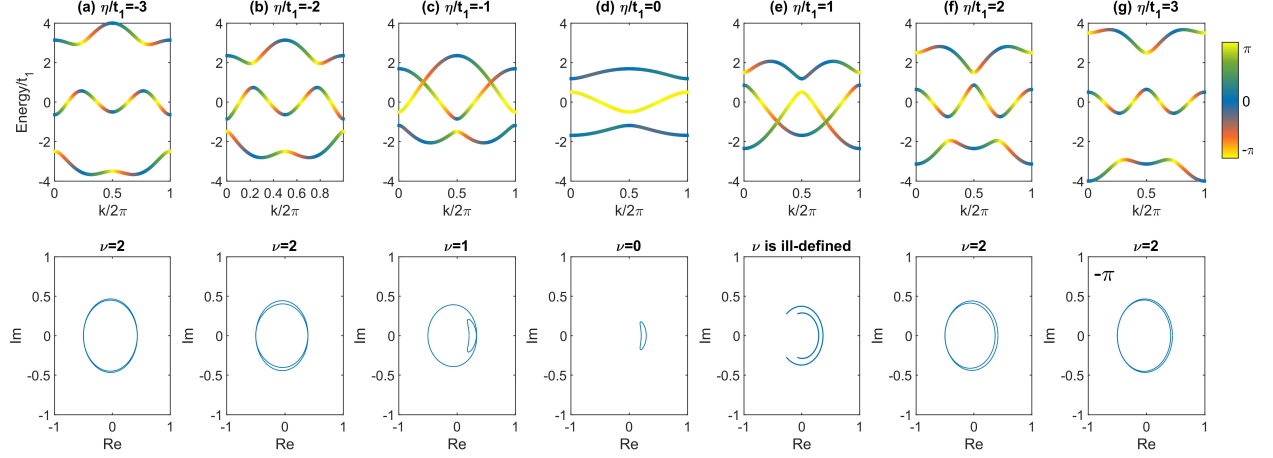


FIG. S1. The band structure (upper panel) and the corresponding inversion winding number of the lowest band (lower panel). The color in the upper panel indicates the winding angle  $\arg q(k) \in [-\pi, \pi)$  at different momenta. Other parameters are the same as the Fig. 1 in the main text.

## S2. REAL-SPACE FORMULA OF THE INVERSION WINDING NUMBER

### A. Equivalence to the momentum-space formula

Here, we prove that the Bott index form of the real-space inversion winding number formula is equivalent to the momentum-space formula in the presence of translation symmetry. First of all, we write the momentum-space formula as an equivalent discretized form:

$$\nu = \frac{1}{2\pi} \text{Im} \sum_k \text{Tr} \left[ \log \left( F_k^{[1]\dagger} F_k^{[3]} \right) \right], \quad (\text{S5})$$

in which  $F_k^{[\sigma]} = \langle u_k | \hat{P}_\sigma | u_{k+\delta k} \rangle$   $\sigma = 1, 2, 3$  and  $\delta k = 2\pi/L$  is the minimal increment of the (quasi) momentum in finite systems. Eq. (S5) is akin to the Wilson loop form and is convenient for numerical computations in finite systems. Notably, the normalization factor is dropped here, as it is a real positive number  $\langle u_k | \hat{P}_\sigma | u_k \rangle \in \mathbb{R}^+$  and does not contribute to the result after taking the imaginary part. For convenience, we only focus on single

gapped band and omit the band index. Then, noting that the projected position matrix  $\mathcal{X}_\sigma = \Psi^\dagger \exp\left(i\frac{2\pi}{L}\hat{x}\right) \hat{P}_\sigma \Psi$  and the Bloch state satisfy:

$$[\mathcal{X}_\sigma]_{k',k} = \langle \psi_{k'} | \exp\left(i\frac{2\pi}{L}\hat{x}\right) \hat{P}_\sigma | \psi_k \rangle = \delta_{k',k+\delta k} \langle u_{k'} | \hat{P}_\sigma | u_k \rangle, \quad (\text{S6})$$

where we have assumed that  $\Psi = (\dots, |\psi_k\rangle, |\psi_{k+\delta k}\rangle, \dots)$  targets the whole band with  $k = 2m\pi/L, m = 1, 2, \dots, L$ . Thus, it can be found that

$$\begin{aligned} [\mathcal{X}_1^\dagger \mathcal{X}_3]_{k',k''} &= \sum_k [\mathcal{X}_1^\dagger]_{k',k} [\mathcal{X}_3]_{k,k''} \\ &= \sum_k \delta_{k',k-\delta k} \delta_{k,k''+\delta k} \langle u_{k-\delta k} | \hat{P}_1 | u_k \rangle \langle u_k | \hat{P}_3 | u_{k-\delta k} \rangle \\ &= \delta_{k',k''} \sum_k \langle u_{k-\delta k} | \hat{P}_1 | u_k \rangle \langle u_k | \hat{P}_3 | u_{k-\delta k} \rangle \\ &= \delta_{k',k''} \sum_k F_{k-\delta k}^{[1]} \left( F_{k-\delta k}^{[3]} \right)^\dagger \end{aligned} \quad (\text{S7})$$

which means the matrix  $\mathcal{X}_1^\dagger \mathcal{X}_3$  is a (block) diagonal matrix and the diagonal term is associated to Eq. (S5). Thus, by taking the matrix logarithm, we then finish the proof:

$$\nu = \frac{1}{2\pi} \text{Im} \sum_k \text{Tr} \left[ \log \left( F_k^{[1]\dagger} F_k^{[3]} \right) \right] = -\frac{1}{2\pi} \text{Im} \left\{ \text{Tr} \left[ \log \left( \mathcal{X}_1^\dagger \mathcal{X}_3 \right) \right] \right\}. \quad (\text{S8})$$

## B. Derivation via the twisted boundary condition

Next, let us introduce the twisted boundary condition (TBC), which serves as a magnetic flux inserting to the system under PBC. The TBC allows us to express the inversion winding number as:

$$\nu = -\frac{1}{\pi} \text{Im} \int_0^{2\pi} d\theta \text{Tr} \left\{ \frac{\Psi_\theta^\dagger \frac{\partial}{\partial \theta} \left[ \left( \hat{P}_3 - \hat{P}_1 \right) \Psi_\theta \right]}{\Psi_\theta^\dagger \left( \hat{P}_1 + \hat{P}_3 \right) \Psi_\theta} \right\}. \quad (\text{S9})$$

Alternatively, one can use the following discrete form of parallel transport for the state:

$$\nu \approx \frac{-1}{2\pi i} \text{Tr} \left\{ \log \left[ \prod_n \left( \Psi_{\theta_n}^\dagger \hat{P}_3 \Psi_{\theta_{n+1}} \right) \left( \Psi_{\theta_n}^\dagger \hat{P}_1 \Psi_{\theta_{n+1}} \right)^\dagger \right] \right\}, \quad (\text{S10})$$

in which we have discretized the twist angle such that  $\theta_1 = 0$  and  $\theta_N = 2\pi$ , and the normalization factor is omitted for simplicity as it does not contribute to the result here. In the presence of translation symmetry, the above formulae are equivalent to the momentum-space form. Moreover, the formula defined through TBC can still work if the translation symmetry is broken while the space-time inversion symmetry is preserved.

Then, to obtain the real-space formula, we need to use the perturbative property of the twist angle in the twisted boundary condition (TBC). As shown in Refs. [S1–S3], there is gauge freedom in the TBC, as the TBC is equivalent to the insertion of magnetic flux to the system in ring geometry. The twist angle attached to the tunneling process across the boundary can be regarded as the effect of vector potential induced by the magnetic field. By appropriately choosing the gauge (called the uniform gauge), the twist angle will be distributed uniformly throughout the system. In this case, the twist angle will be threaded to all tunneling process with a strength of  $\theta/L$ , which is an extremely small quantity if  $L \rightarrow \infty$ . To obtain the uniform gauge, we can introduce the following twist operator

$$\hat{U}_\theta = \exp\left(i\frac{\theta}{L}\hat{x}\right), \quad (\text{S11})$$

where  $\hat{x}$  is the position operator. The Hamiltonian under conventional TBC can be transformed to the uniform-gauge form (labelled by tilde notation):

$$\tilde{H}(\theta) = \hat{U}_\theta \hat{H}(\theta) \hat{U}_\theta^{-1}. \quad (\text{S12})$$

The system satisfies the gauge-invariant condition:

$$\begin{aligned} \hat{H}(\theta + 2\pi) &= \hat{H}(\theta) \\ \tilde{H}(\theta + 2\pi) &= \hat{U}_{2\pi} \tilde{H}(\theta) \hat{U}_{2\pi}^{-1}. \end{aligned} \quad (\text{S13})$$

Under the uniform gauge, we can treat  $\theta/L$  as a perturbation and expand the Hamiltonians and the eigenstates. There is

$$\tilde{\Psi}_\theta = \tilde{\Psi}_0 + \frac{\theta}{L} \left( \frac{\partial}{\partial(\theta/L)} \tilde{\Psi}_\theta \right)_{\theta=0} + O\left(\frac{1}{L^2}\right). \quad (\text{S14})$$

By substituting it into the expression of inversion winding number and keeping up to the leading order of  $1/L$ , we have

$$\begin{aligned} \nu &= -\frac{1}{\pi} \text{Im} \int_0^{2\pi} d\theta \text{Tr} \left\{ \frac{\tilde{\Psi}_\theta^\dagger \frac{\partial}{\partial\theta} \left[ (\hat{P}_3 - \hat{P}_1) \tilde{\Psi}_\theta \right]}{\tilde{\Psi}_\theta^\dagger (\hat{P}_1 + \hat{P}_3) \tilde{\Psi}_\theta} \right\} \\ &\approx -\frac{1}{\pi} \text{Im} \int_0^{2\pi} d\theta \text{Tr} \left[ \frac{\tilde{\Psi}_0^\dagger (\hat{P}_3 - \hat{P}_1) \left( \frac{\partial}{\partial\theta} \tilde{\Psi}_\theta \right)_{\theta=0}}{\tilde{\Psi}_0^\dagger (\hat{P}_1 + \hat{P}_3) \tilde{\Psi}_0} \right] \\ &= -2\text{Im} \left\{ \text{Tr} \left[ \frac{\tilde{\Psi}_0^\dagger (\hat{P}_3 - \hat{P}_1) \left( \frac{\partial}{\partial\theta} \tilde{\Psi}_\theta \right)_{\theta=0}}{\tilde{\Psi}_0^\dagger (\hat{P}_1 + \hat{P}_3) \tilde{\Psi}_0} \right] \right\} \end{aligned} \quad (\text{S15})$$



According to Eq. (S13), the eigenstates will follow the same relations:

$$\tilde{\Psi}_{2\pi} = \hat{U}_{2\pi} \tilde{\Psi}_0 \quad (\text{S16})$$

given that the target eigenstates are gapped. Thus, we can approximate the partial derivative

$$\begin{aligned} \left( \frac{\partial}{\partial \theta} \tilde{\Psi}_\theta \right)_{\theta=0} &\approx \frac{1}{2\pi} \left( \tilde{\Psi}_{2\pi} - \tilde{\Psi}_0 \right) \\ &= \frac{1}{2\pi} \left( \hat{U}_{2\pi} \tilde{\Psi}_0 - \tilde{\Psi}_0 \right). \end{aligned} \quad (\text{S17})$$

Therefore the expression of the inversion winding number can be further approximated to:

$$\nu \approx -\frac{1}{\pi} \text{Im} \left\{ \text{Tr} \left[ \frac{\Psi_0^\dagger \left( \hat{P}_3 - \hat{P}_1 \right) \left( \hat{U}_{2\pi} \Psi_0 - \Psi_0 \right)}{\tilde{\Psi}_0^\dagger \left( \hat{P}_1 + \hat{P}_3 \right) \tilde{\Psi}_0} \right] \right\} \quad (\text{S18})$$

where we have used the fact that  $\text{Im} \left\{ \text{Tr} \left[ \Psi_0^\dagger \left( \hat{P}_3 - \hat{P}_1 \right) \Psi_0 \right] \right\} = 0$ . Then, we further expand the twisted operator such that

$$\hat{U}_{2\pi} = \exp \left( i \frac{2\pi}{L} \hat{x} \right) \approx \hat{I} + i \frac{2\pi}{L} \hat{x}. \quad (\text{S19})$$

Finally, after these approximations, we obtain the following real-space formula

$$\nu \approx -\frac{2}{L} \text{Tr} \left[ \frac{\Psi_0^\dagger \left( \hat{X}_3 - \hat{X}_1 \right) \hat{x} \Psi_0}{\Psi_0^\dagger \left( \hat{P}_1 + \hat{P}_3 \right) \Psi_0} \right] \quad (\text{S20})$$

which clearly shows that the inversion winding number describes the polarization difference between sublattices upon normalization. It is worth noting that Eq. (S20) works for bulk states in the gapped band. In fact, this approximation is poor under PBC, as the convergence is slow. Nevertheless, when the system is under the OBC, the edge state and the bulk state are separated. By applying Eq. (S20) respectively for the bulk states and the edge states yield satisfactory results, as already shown in the main text. Interestingly, the bulk states and the edge states approximately have the opposite polarization profile in real space. We would like to point out that the edge state is degenerate under OBC and they are equally contributed from the lower and upper bands. Thus, when targeting the edge states, we need to distinguish them. This yields the expression for the edge state in the main text. Notably, the real-space formula is affected by the band gap, since we have treated the twist angle as a perturbation. This explains why the real-space formula produces a result deviating from the quantized value.

On the other hand, the Bott index form of the real-space inversion winding number can be also derived through the TBC. The derivation is reminiscent to that in Ref. [S1]. With Eq. (S10), we leverage the perturbative nature of the twist angle and approximate the product as

$$\begin{aligned}\nu &\approx -\frac{1}{2\pi i} \text{Tr} \left\{ \log \left[ \left( \tilde{\Psi}_0^\dagger \hat{P}_3 \tilde{\Psi}_{2\pi} \right) \left( \tilde{\Psi}_0^\dagger \hat{P}_1 \tilde{\Psi}_{2\pi} \right)^\dagger \right] \right\} \\ &= -\frac{1}{2\pi} \text{Im} \left\{ \text{Tr} \left[ \log \left( \mathcal{X}_1^\dagger \mathcal{X}_3 \right) \right] \right\},\end{aligned}\quad (\text{S21})$$

which is exactly the real-space formula of the inversion winding number appearing in the main text.

### C. In views of the Wannier state

We can construct the Wannier state localized at  $R$  via the superposition of Bloch states

$$|w(R)\rangle = \frac{1}{\sqrt{L}} \sum_k e^{-ikR} |\psi_k\rangle = \frac{1}{\sqrt{L}} \sum_k e^{-ikR} \sum_{x,\sigma} u_{k,\sigma} e^{ikx} |x, \sigma\rangle. \quad (\text{S22})$$

The center of the Wannier state is known to related to the polarization

$$\langle w(R) | \hat{x} | w(R) \rangle \approx \frac{1}{2\pi} \int_0^{2\pi} dk \langle u_k | i\partial_k u_k \rangle. \quad (\text{S23})$$

It is worth noting that we can decompose the Wannier state into different sublattice sectors.

The Wannier centers in different sublattices read as

$$\begin{aligned}\langle w(R) | \hat{x} \hat{P}_\sigma | w(R) \rangle &= R \sum_k u_{k,\sigma}^* u_{k,\sigma} + \sum_k u_{k,\sigma}^* i\partial_k u_{k,\sigma} \\ &\approx \frac{R}{2\pi} \int_0^{2\pi} dk \langle u_k | \hat{P}_\sigma | u_k \rangle + \frac{1}{2\pi} \int_0^{2\pi} dk \langle u_k | \hat{P}_\sigma i\partial_k u_k \rangle.\end{aligned}\quad (\text{S24})$$

Clearly, the inversion winding number reflects the relative polarization between sublattices in the Wannier state:

$$\nu \propto \langle w(R) | \hat{x} \left( \hat{P}_3 - \hat{P}_1 \right) | w(R) \rangle. \quad (\text{S25})$$

### D. More information on the phase diagram in the presence of disorder

Here, we supplement some more data about the phase diagram in the presence of inversion-invariant disorder. In Fig. S2, we present the first gap (b) and the standard

deviation of the inversion winding number (c) numerically. It can be seen that the finite spectral gap only survives for weak disorder ( $W/t_1 \ll 1$ ). For strong disorder ( $W/t_1 \gg 1$ ), the energy gap between the first and the second band is vague near the phase transition area. However, in those area where the inversion winding number fluctuate less, we can still distinguish a small finite energy gap, see Fig. S2 (d-e) for example. According to the diagram of the standard deviation, one can clearly find wide and stable areas with extremely small fluctuation even if the spectral gap is small. The disorder-induced topological phase transition is signified by large fluctuations of the inversion winding number, which highlights the phase boundary. Also, it can be seen from the spectrum in Fig. S2 (d-e) that the change of edge states are consistent to the inversion winding number and the gap closing point. This clearly reflects the principle of bulk-edge correspondence.

For completeness, we present the phase diagram of the inversion winding number for all three bands in Fig. S3 with the same parameters. It can be clearly seen that inversion winding numbers of the three bands still satisfy the relation:  $\nu_{n=2} = \nu_{n=1} + \nu_{n=3}$ . The phase transition boundaries for two adjacent bands are well consistent. This means that the topological phases in this three-band system protected by the space-time inversion symmetry are stable for strong symmetry-invariant disorders. These results further evidence that the inversion winding number is capable to depict the band topology in such kind of systems.

### S3. BULK-EDGE CORRESPONDENCE AND THE INVERSION WINDING NUMBER

In this section, we discuss the bulk-edge correspondence for the inversion winding number. To relate the inversion winding number to the edge state, one of the prominent approaches is through the twisted boundary condition (TBC), which has been applied in many topological systems to study the bulk-edge correspondence [S1, S4, S5]. Under TBC, wavefunctions satisfy the relation:  $\psi(x + L) = \exp(i\theta) \psi(x)$ , in which  $L$  is the number of cells and  $m$  is the number of sublattices. It can be verified that the inversion symmetry yields:  $\hat{\mathcal{I}}\hat{H}(\theta)\hat{\mathcal{I}}^{-1} = \hat{H}(\theta)^*$ .

In analogy to the momentum-space method [Eq. (S1)], we can define the  $L \times L$  matrix:

$$q(\theta) = \Psi_\theta^\dagger \hat{\mathcal{P}}_{3,1} \Psi_\theta, \quad (\text{S26})$$

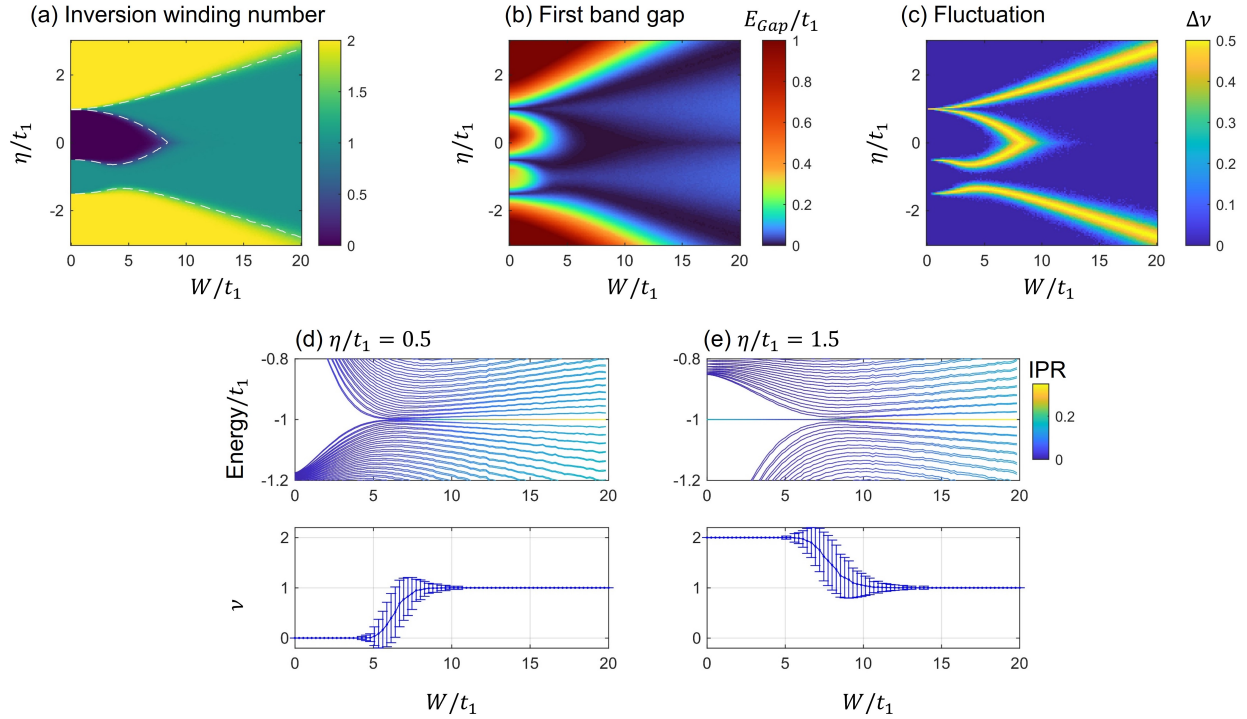


FIG. S2. (a-c):  $\eta - W$  phase diagram of: (a) inversion winding number (already presented in the main text), (b) first spectral gap, and (c) the standard deviation of the inversion winding number among different realizations:  $\Delta\nu = \sqrt{\sum_{i=1}^N (\nu^{(i)} - \bar{\nu})^2 / N}$ . Dashed lines indicate the phase boundary. (d-e): spectrum near the first gap and the inversion winding number of the first band along (d)  $\eta/t_1 = 0.5$  and (e)  $\eta/t_1 = 1.5$ . The change of edge states number (resolved by distinct inverse participation ratio) are: (d)  $N_{edge} = 0 \rightarrow N_{edge} = 2$  and (e)  $N_{edge} = 4 \rightarrow N_{edge} = 2$ . Error bars indicate the standard deviation. The number of cell is chosen as  $L = 200$  and each data is averaged over  $10^3$  random realizations.

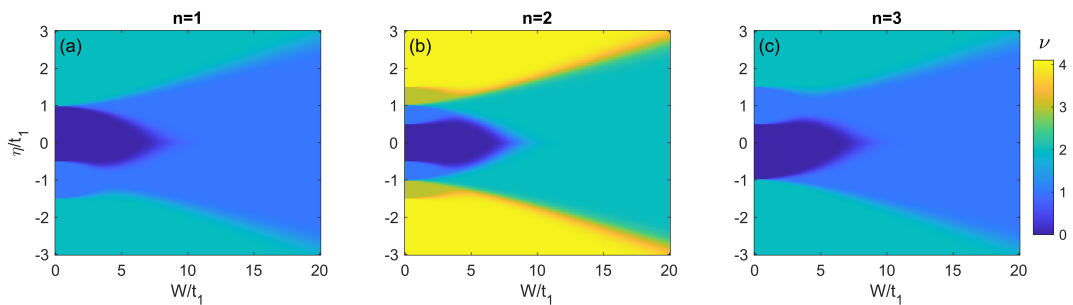


FIG. S3.  $\eta$ - $w$  phase diagram of inversion winding number for all three bands. Parameters are the same as Fig. S3.



where  $\Psi_\theta = (|\psi_1(\theta)\rangle, \dots, |\psi_{\mathcal{N}}(\theta)\rangle)$  collects eigenvectors on the target band under TBC and  $\hat{\mathcal{P}}_{1,3} = \sum_x |x, 1\rangle\langle x, 3|$ . The inversion winding number can be written as

$$\nu = -\frac{1}{2\pi} \int_0^{2\pi} d\theta \operatorname{Tr} [q(\theta)^{-1} \partial_\theta q(\theta)]. \quad (\text{S27})$$

Notably, through the singular value decomposition, the  $q$  matrix in Eq. (S26) can be also written as a product of two  $L \times L$  matrices such as  $q(\theta) = u^\dagger(\theta)v(\theta)$ . Their matrix elements can be explicitly written as

$$[u(\theta)]_{x,m} = \langle x, 1 | \psi_m(\theta) \rangle, \quad [v(\theta)]_{x,m} = \langle x, 3 | \psi_m(\theta) \rangle, \quad (\text{S28})$$

in which  $m$  is the index of eigenstate. Since we are focusing on a single gapped band, the number of eigenstates here is  $L$  as well. In the presence of PBC, the eigenstate can be written as the Bloch function

$$|\psi_{n,k}\rangle = \sum_\sigma u_{n,k}^\sigma |k, \sigma\rangle = \sum_\sigma u_{n,k}^\sigma e^{ikx} |x, \sigma\rangle. \quad (\text{S29})$$

For the three-band system with space-time inversion symmetry, there is:

$$\begin{aligned} \langle 1, x | \psi_{n,k} \rangle &= \alpha_k e^{-i\xi_k} e^{ikx}, \\ \langle 3, x | \psi_{n,k} \rangle &= \alpha_k^* e^{ikx} \end{aligned} \quad (\text{S30})$$

In this condition, all columns of matrix  $u(0)$  or  $v(0)$  are mutually orthogonal (but not normalized) provided that the band is gapped and  $\alpha_k \neq 0$ . Since the number of these columns is equal to the dimension of the matrix, they form a complete set in this subspace. Thus, we can conclude that these matrices are non-singular under PBC. This property should remain for  $\theta \neq 0$  as long as the band gap is still finite since the twist angle only act as a  $1/L$ -order perturbation [S1, S3, S6].

Next, we multiply a real parameter  $r \in [0, 1]$  on the tunnelings across the boundary, which is introduced in the main text. Then,  $r = 0$  corresponds to the OBC and  $r = 1$  corresponds to the general TBC. By changing the value of  $r$ , we are able to continuously connect the TBC to OBC. With these configurations, the translation symmetry is broken while the inversion symmetry is still preserved. Hence, the winding numbers in Eq. (S27) can be well defined for  $r < 1$  if these eigenstates are well gapped to other bands. The inversion winding number is equivalent to the following closed integral on a complex plane:

$$\nu = \frac{1}{2\pi} \oint_{r=1} \frac{dz}{z}, \quad (\text{S31})$$

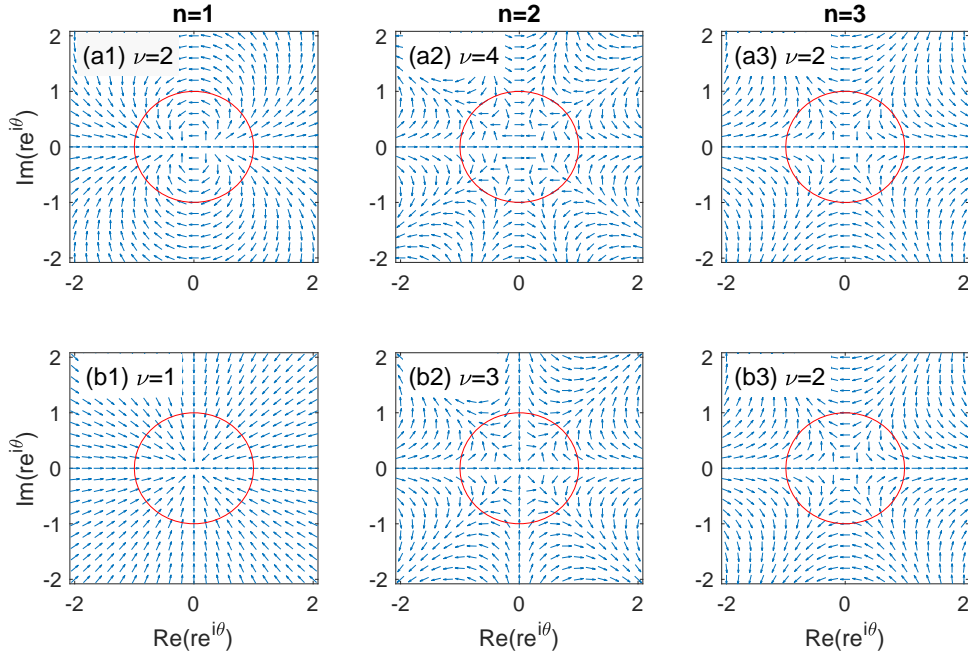


FIG. S4. Distribution of the complex number  $\det q(\theta, r)$  on the complex plane for  $n = 1$  to  $n = 3$  bands. (a) and (b) respectively corresponds to  $\eta/t_1 = 2$  and  $\eta/t_1 = -1.2$ . Red line indicates the  $r = 1$  circle, corresponding to normal TBC. Other parameters are set to:  $t_2/t_1 = 0.5$  and  $L = 50$ .

in which we define  $z \equiv \det q(r, \theta) \in \mathbb{C}$ . Non-trivial winding number under PBC implies that there are residues of the complex function  $f(z) = z^{-1}$  insider the  $r = 1$  circle. This means that the matrix  $q(r, \theta)$  becomes singular at some points  $r \in [0, 1)$  and  $\theta \in [0, 2\pi]$ . On the one hand, since the twist angle  $\theta$  is only a perturbative parameter in order of  $1/L$ , which is an extremely small quantity in the thermodynamic limit, we can conclude that finite singular points should only reside at  $r = 0$  in the thermodynamic limit. Otherwise, there are numerous singular points for  $\theta \in [0, 2\pi]$ . Similar to the case in 1D chiral-symmetric topological insulators, we find that the singularity is caused by the some degenerate eigenstates among two different bands. For two gapped bands, the spectral gap should be both finite under OBC and PBC, except that some finite in-gap states may emerge from the band. It is this degeneracy that causes the singularity if we continuously change the boundary condition from TBC to OBC. Thus, we can infer that the singularity of the  $q$  matrix is associated to these degenerate in-gap edge states under OBC ( $r = 0$ ). The number of these in-gap states is directly related to the inversion winding number, which constitutes the principle of bulk-edge correspondence here.

## Numerical results

Next, we present the numerical calculation for the complex number  $\det q(\theta, r)$  in Fig. S4. The inversion winding number under TBC can be easily extracted from the winding of  $\det q(\theta, r)$ . Here we have set  $t_2/t_1 = 1/2$  and set  $\eta/t_1 = 2$  in (a1-a3) and  $\eta/t_1 = -1.2$  in (b1-b3). In both instances, the inversion winding number among these three bands are  $\nu_{n=2} = \nu_{n=1} + \nu_{n=3}$ . Moreover, it can be identified that the singular point resides at the  $r = 0$ . This is consistent to our previous conclusion that the appearance of degenerate in-gap edge states is the result of non-trivial band topology.

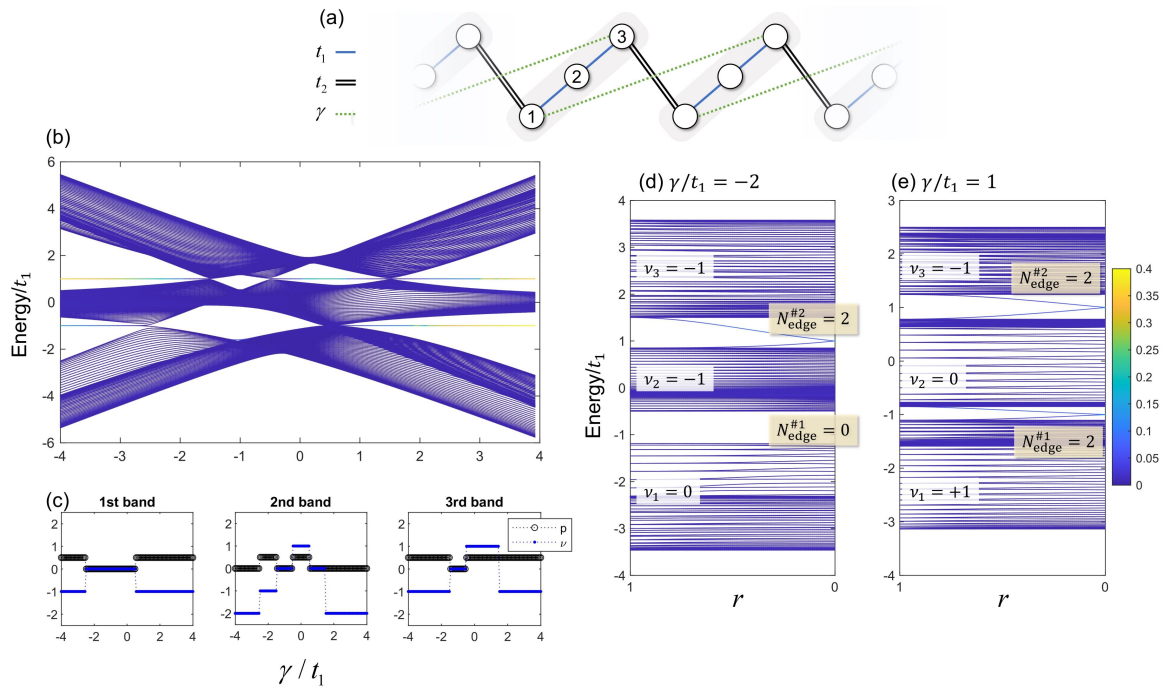


FIG. S5. (a) Schematic illustration of the tunneling  $\gamma$ . The  $\eta$  term is not shown here for conciseness. (b) Energy spectrum as a function of  $\gamma/t_1$  under OBC. Other parameters are chosen as:  $t_2/t_1 = 1$ ,  $\eta/t_1 = 0.5$  and  $L = 100$ .

To complete the discussions on the bulk-edge correspondence, we add a tunneling between first and third sublattice, as depicted in Fig. S5 (a). This allows for a  $\nu < 0$  topological phase. The complex parameter  $h_k$  in the Bloch Hamiltonian reads as:  $h_k = -t_2 e^{-ik} - \eta e^{-2ik} - \gamma e^{ik}$ . We then compute the energy spectrum under OBC and the topological invariant under PBC, as shown in Fig. S5 (b-c). It can be seen that there appears the  $\nu = -1$  phase due to the  $\gamma$  tunneling. The inversion winding number among the three bands still satisfy:  $\nu_2 = \nu_1 + \nu_3$ .

The number of edge states is also proportional to the inversion winding number in the first or the third band. By inspecting the spectral flow as a function of parameter  $r$  in Fig. S5 (d-e), we again clearly see that the number of edge states emerging from the band is related to the band inversion winding number. Quite different from the cases in the main text, it turns out that the inversion winding number of the second band is zero in Fig. S5 (e), while there still appears the in-gap edge states. This is because the second band consists of two opposite inversion winding number, leading to the total zero value. This result is still consistent to the bulk-edge correspondence of the inversion winding number discussed above.

#### S4. SPACE-TIME INVERSION SYMMETRY AND QUANTIZATION OF TOPOLOGICAL INVARIANTS

##### A. Quantization of the polarization (Berry-Zak phase)

With the space-time inversion symmetry  $\mathcal{I}H(k)\mathcal{I}^{-1} = H(k)^*$ , we here show that the Berry phase of gapped band is quantized to 0 or  $\pi$  modulo  $2\pi$ . Firstly, note that  $\mathcal{I}|u_k\rangle = |(u_k)^*\rangle$ , where  $|u_k\rangle$  is eigenstate of the  $H(k)$  while  $|(u_k)^*\rangle$  is eigenstate of the  $H(k)^*$ . The polarization of a gapped band reads as

$$p = \frac{i}{2\pi} \int_0^{2\pi} dk \langle u_k | \partial_k u_k \rangle \pmod{1}. \quad (\text{S32})$$

Inserting  $\mathcal{I}^2 = 1$  onto this expression, we find

$$\begin{aligned} p &= \frac{i}{2\pi} \int_0^{2\pi} dk \langle u_k | \mathcal{I} \mathcal{I} \partial_k u_k \rangle \pmod{1} \\ &= \frac{i}{2\pi} \int_0^{2\pi} dk \langle (u_k)^* | \partial_k (u_k)^* \rangle \pmod{1} \\ &= \frac{i}{2\pi} \int_0^{2\pi} dk \langle \partial_k u_k | u_k \rangle \pmod{1}. \end{aligned} \quad (\text{S33})$$

Combining Eq. (S32) and Eq. (S33) and using  $\partial_k (\langle u_k | u_k \rangle) = \langle \partial_k u_k | u_k \rangle + \langle u_k | \partial_k u_k \rangle = 0$ , one finds that  $(p + p) \pmod{1} = 0$ . Thus, we conclude that in the presence of space-time inversion symmetry the polarization can only be 0 or  $1/2$  modulo 1. In fact, the inversion symmetry can solely quantize the polarization.



## B. Quantization of the inversion winding number and its relation to the polarization

In the main text, we have defined inversion winding numbers for three-band topological crystalline insulators. Here, we show that the the inversion winding numbers are related to the band polarization such that  $p = \nu/2 \pmod{1}$ . In three-band systems with the inversion symmetry, the normalized eigenvector can be written as

$$u_k = \begin{pmatrix} \alpha_k e^{-i\xi_k} \\ \beta_k e^{-i\frac{\xi_k}{2}} \\ \alpha_k^* \end{pmatrix}. \quad (\text{S34})$$

It can be found that

$$\begin{aligned} \int_0^{2\pi} dk (u_k^\dagger i \partial_k u_k) &= \int_0^{2\pi} dk (\alpha_k^* i \partial_k \alpha_k) + \int_0^{2\pi} dk (\beta_k^* i \partial_k \beta_k) \\ &+ \int_0^{2\pi} dk (\alpha_k i \partial_k \alpha_k^*) + \int_0^{2\pi} dk \left[ \left( |\alpha_k|^2 + \frac{1}{2} |\beta_k|^2 \right) \partial_k \xi_k \right]. \end{aligned} \quad (\text{S35})$$

By using the normalization relation, we have  $2|\alpha_k|^2 + |\beta_k|^2 = 1$ . Thus, one finds the following relation:

$$p = \frac{1}{2\pi} \int_0^{2\pi} dk (u_k^\dagger i \partial_k u_k) = \frac{1}{2} \int_0^{2\pi} dk \partial_k \xi_k \in \frac{\mathbb{Z}}{2}. \quad (\text{S36})$$

which again proves the quantization of Berry phase modulo  $2\pi$ . These results reflect the importance of the phase factor  $\xi_k$  in the space-time inversion-symmetric topological insulators. Then, according to Eq. (S34), we can expand the inversion winding number:

$$\begin{aligned} \nu &= \frac{1}{\pi i} \text{Im} \int_0^{2\pi} dk \left[ \frac{\langle u_k | \frac{\partial}{\partial k} (\hat{P}_3 - \hat{P}_1) u_k \rangle}{\langle u_k | \hat{P}_1 + \hat{P}_3 | u_k \rangle} \right] \\ &= \frac{1}{\pi i} \int_{B.Z.} dk \frac{\alpha_k \frac{\partial}{\partial k} (\alpha_k^*) - (\alpha_k e^{-i\xi_k})^* \frac{\partial}{\partial k} (\alpha_k e^{-i\xi_k})}{2|\alpha_k|^2} \\ &= \frac{1}{\pi i} \int_{B.Z.} dk \frac{\alpha_k \frac{\partial}{\partial k} (\alpha_k^*)}{|\alpha_k|^2} + \frac{1}{2\pi i} \int_{B.Z.} dk (e^{i\xi_k})^* \frac{\partial}{\partial k} (e^{i\xi_k}) \\ &= 2\nu_\alpha + \nu_\xi, \end{aligned} \quad (\text{S37})$$

where we have denoted two integer numbers

$$\begin{aligned}\nu_\alpha &= \frac{1}{2\pi i} \int_{B.Z.} dk \frac{\alpha_k \frac{\partial}{\partial k} (\alpha_k^*)}{|\alpha_k|^2} \in \mathbb{Z} \\ \nu_\xi &= \frac{1}{2\pi i} \int_{B.Z.} dk (e^{i\xi_k})^* \frac{\partial}{\partial k} (e^{i\xi_k}) = \int_0^{2\pi} dk \partial_k \xi_k \in \mathbb{Z}.\end{aligned}\quad (\text{S38})$$

Compared to Eq. (S36), we can immediately obtain the relation between the inversion winding number  $\nu$  and the polarization  $p$ :

$$\frac{\nu}{2} \bmod 1 = p. \quad (\text{S39})$$

It is worth noting that, even though the inversion winding number may become ill-defined if  $\alpha_k = 0$  while the spectral gap is not closed, we can always add some perturbative terms to let  $\alpha_k \neq 0$ . In this sense, the inversion winding number is at least a  $\mathbb{Z}_2$  topological invariant. As mentioned in the main text, by further imposing constraints on the form of Hamiltonian, the inversion winding number becomes the topologically stable  $\mathbb{Z}$  topological invariant.

## S5. REAL-SPACE MODEL AND EXPERIMENTAL REALIZATION

In this section, we discuss the three-band model in 1D presented in the main text. By transforming the Bloch Hamiltonian to real space, we obtain the following tight-binding second-quantized form

$$\hat{H} = -t_1 \sum_j \left( \hat{a}_{2,j}^\dagger \hat{a}_{1,j} + \hat{a}_{3,j}^\dagger \hat{a}_{1,j} \right) - t_2 \sum_j \hat{a}_{3,j}^\dagger \hat{a}_{1,j+1} - \eta \sum_j \hat{a}_{3,j}^\dagger \hat{a}_{1,j+2} + \text{H.c.}, \quad (\text{S40})$$

where  $\hat{a}_{\sigma,j}^\dagger$  represents the particle creation operation at  $\sigma = 1, 2, 3$  sublattice in the  $j$ th cell. We present two equivalent real-space illustrations in Fig. S6. Fig. S6 (a) shows a general configuration of 1D zigzag chain.  $t_1$  and  $t_2$  terms manifest as the nearest-neighbor tunneling while the  $\eta$  terms correspond to the long-range tunneling. We can modify the configuration and consider a equivalent ladder-like model, see Fig. S6 (b). In this ladder-like model, the long-range tunneling is arranged in a relatively short-range manner, which provides a more convenient approach for experimental realizations.

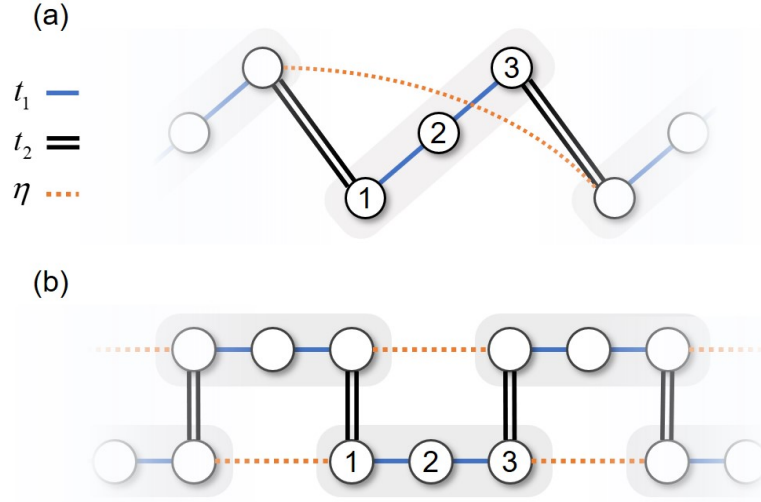


FIG. S6. Schematic illustration of the 1D three-band model in real space. (a) and (b) are equivalent.

### A. Measurement from the edge states

Since the in-gap edge states are degenerate, their arbitrary linear combinations are still the eigenstates of the system. Nevertheless, the overall density distribution of these in-gap edge states is unique and it is possible to observe experimentally. For example, the edge state can be excited selectively in acoustic systems [S7, S8] by varying the energy. To detect the inversion winding number through the density distribution of the edge state, we can write the real-space formula for the edge state presented in the main text as the following convenient form

$$\nu = \frac{\mathcal{D}_{\text{edge}}}{L} \frac{\sum_x x (\bar{n}_{x,3} - \bar{n}_{x,1})}{\sum_x (\bar{n}_{x,3} + \bar{n}_{x,1})}, \quad (\text{S41})$$

where  $\bar{n}_{x,\sigma}$  represents the density distribution at  $\sigma$  lattice of the  $x$ th cell and  $\mathcal{D}_{\text{edge}}$  is the degeneracy of the edge state. Here we have assumed that the density distribution is normalized to identity:  $\sum_{x,\sigma} \bar{n}_{x,\sigma} = 1$ . It is worth noting that, in experiment, the degeneracy of the edge state  $\mathcal{D}_{\text{edge}}$  is not obvious when measuring the density distribution. In finite systems, the degeneracy may be lifted due to the large localization length of edge states, which offers possibility for resolving them. On the other hand, even though the degeneracy is not lifted, we can manually add some extra terms to slightly break the degeneracy and then we can measure the winding number for different edge states.

## B. Measurement from the bulk states

As for the measurement through the bulk state, it is generally difficult to directly probe the density distribution of them. However, it is possible to realize it via the dynamical evolution. Suppose that we can prepare a state being the superposition of the bulk state in a given band, the time evolution of this state yields

$$|\Psi(t)\rangle = \sum_{n \in \text{target}} e^{-iE_n t} c_n |\psi_n\rangle. \quad (\text{S42})$$

The expectation of the operator  $\hat{O}$  reads as

$$\bar{O}(t) = \sum_{n, n' \in \text{target}} e^{-i(E_n - E_{n'})t} c_{n'}^* c_n \langle \psi_{n'} | \hat{O} | \psi_n \rangle. \quad (\text{S43})$$

By averaging over time, we have

$$\frac{1}{T} \int_0^T dt \bar{O}(t) = \sum_{n, n' \in \text{target}} \left[ \frac{1}{T} \int_0^T dt e^{-i(E_n - E_{n'})t} \right] c_{n'}^* c_n \langle \psi_{n'} | \hat{O} | \psi_n \rangle. \quad (\text{S44})$$

If the evolution time is sufficiently long  $T \rightarrow \infty$ , we approximately have

$$\frac{1}{T} \int_0^T dt \bar{O}(t) \approx \sum_{n \in \text{target}} |c_n|^2 \langle \psi_n | \hat{O} | \psi_n \rangle, \quad (\text{S45})$$

which means that the long-time average leads to the ensemble average. Thus, by selecting the appropriate initial state, we can accomplish the measurement of the topological invariant from bulk states.

It can be seen that the most important step is to prepare the proper initial state on the certain band. To realize it, we consider a adiabatic preparation. By adding the following extra potential to break the inversion symmetry:

$$\hat{H}_\Delta = \Delta \sum_x (\hat{n}_{x,3} - \hat{n}_{x,1}), \quad (\text{S46})$$

the three bands will be well separated by large energy difference  $\Delta \gg 0$  and the system is approximately in the atomic limit. Thus, it is quite easy to prepare the desired state as the superposition of the bulk states on certain band by using the Fock state localized in certain site. Then, we can slowly reduce the extra potential to zero. Finally, this state will greatly overlap with the target band. Then we let this state evolve and measure according to the formula of the inversion winding number, which leads to the results in Fig. 4 (b) in the main text.

## S6. MORE SYSTEMS

In order to better understand the essential role of relative phase difference (polarization) between sublattices (orbitals), here we analyze the two- and four-band systems in the presence of space-time inversion symmetry and explore the band topology of them.

### A. Two-band systems

Firstly, let us consider the two-band case, which is a bipartite lattice consisting of two sublattices. In the presence of the space-time inversion symmetry, the Bloch Hamiltonian reads as

$$H(k) = \begin{pmatrix} g_k & h_k \\ h_k^* & g_k \end{pmatrix}, \quad \mathcal{I} = \begin{pmatrix} 0 & 1 \\ 1 & 0 \end{pmatrix}, \quad (\text{S47})$$

which satisfies  $\sigma_x H(k) \sigma_x = H(k)^*$ . It can be found that the system possesses the chiral symmetry when  $g_k = 0$ . In fact, the Hamiltonian can be separated into two parts, namely the chiral part and the identity part

$$H(k) = H_{\text{chiral}}(k) + g_k I_{2 \times 2}. \quad (\text{S48})$$

These two terms commute with each other. Therefore, the eigenstate of the inversion-symmetric system here has the same eigenstate as the chiral-symmetric one, which is classified by  $\mathbb{Z}$ . For example, this Bloch Hamiltonian can be easily diagonalized:

$$\begin{aligned} E_{\pm, k} &= g_k \pm |h_k|, \\ \psi_{\pm, k} &= \frac{1}{\sqrt{2}} \begin{pmatrix} e^{-i \arg |h_k|} \\ \pm 1 \end{pmatrix}. \end{aligned} \quad (\text{S49})$$

Since the identity part only brings a constant shift to the eigenenergy, the energy gap and the eigenvector of  $H(k)$  is not affected. Hence, we expect that the inversion-symmetric system should share the same topology with the chiral-symmetric one.

### B. Four-band systems

As another concrete example, we study a family of four-band systems with the space-time inversion symmetry, which host much more complicated topological phases. The space-time

inversion symmetry discussed in the main text requires the following form of the Bloch Hamiltonian:

$$H(k) = \begin{pmatrix} \Delta & \gamma_k & \lambda_k & g_k \\ \gamma_k^* & -\Delta & h_k & \lambda_k \\ \lambda_k^* & h_k^* & -\Delta & \gamma_k \\ g_k^* & \lambda_k^* & \gamma_k^* & \Delta \end{pmatrix}, \quad \mathcal{I} = \begin{pmatrix} & & & 1 \\ & & & \\ & & 1 & \\ & & & \\ 1 & & & \end{pmatrix}, \quad (\text{S50})$$

in which  $\Delta_k \in \mathbb{R}$ ,  $\gamma_k, \lambda_k, g_k, h_k \in \mathbb{C}$ . The symmetry constraint imposes strong constraint on the eigenvector of  $H(k)$ , which can be written as the following general form:

$$u_k = \begin{pmatrix} \alpha_k e^{-i\xi_k} \\ \beta_k e^{-i\xi_k} \\ \beta_k^* \\ \alpha_k^* \end{pmatrix}, \quad (\text{S51})$$

which is similar to the three-band case. Again, the phase factor  $\exp(-i\xi_k)$  cannot be totally gauged out. Similarly, it can be checked that  $(\mathcal{I}u_k)^* = e^{i\xi_k}u_k$ .

Next, we seek for possible definitions of the winding number within this inversion-symmetric system. Unlike the three-band case, we need to introduce two inversion winding numbers to determine the topology according to the number of parameters in the eigenvector:

$$\begin{aligned} \nu_\alpha &= \frac{1}{\pi i} \int_0^{2\pi} dk \left[ \frac{\langle u_k | \frac{\partial}{\partial k} (\hat{P}_4 - \hat{P}_1) u_k \rangle}{\langle u_k | \hat{P}_1 + \hat{P}_4 | u_k \rangle} \right], \\ \nu_\beta &= \frac{1}{\pi i} \int_0^{2\pi} dk \left[ \frac{\langle u_k | \frac{\partial}{\partial k} (\hat{P}_3 - \hat{P}_2) u_k \rangle}{\langle u_k | \hat{P}_2 + \hat{P}_3 | u_k \rangle} \right]. \end{aligned} \quad (\text{S52})$$

To change values of the winding numbers above, there must be  $\alpha_k = 0$  or  $\beta_k = 0$  at some momentum  $k$ . Hence, it is of importance to know in what condition that  $\alpha_k = 0$  or  $\beta_k = 0$ . Firstly, let us assume that  $\alpha_k = 0$  and solve the eigenvalue equation  $H(k)\psi_k = E_k\psi_k$ . The eigenvector should obey:

$$\begin{pmatrix} \Delta_k & \gamma_k & \lambda_k & g_k \\ \gamma_k^* & -\Delta_k & h_k & \lambda_k \\ \lambda_k^* & h_k^* & -\Delta_k & \gamma_k \\ g_k^* & \lambda_k^* & \gamma_k^* & \Delta_k \end{pmatrix} \begin{pmatrix} 0 \\ \beta_k e^{-i\xi_k} \\ \beta_k^* \\ 0 \end{pmatrix} = \begin{pmatrix} \gamma_k \beta_k e^{-i\xi_k} + \lambda_k \beta_k^* \\ \Delta_k \beta_k e^{-i\xi_k} + h_k \beta_k^* \\ h_k^* \beta_k e^{-i\xi_k} + \Delta_k \beta_k^* \\ \lambda_k^* \beta_k e^{-i\xi_k} + \gamma_k^* \beta_k^* \end{pmatrix} = E_k \begin{pmatrix} 0 \\ \beta_k e^{-i\xi_k} \\ \beta_k^* \\ 0 \end{pmatrix}, \quad (\text{S53})$$



which requires that

$$\begin{aligned}\gamma_k \beta_k e^{-i\xi_k} + \lambda_k \beta_k^* &= 0; \\ \lambda_k^* \beta_k e^{-i\xi_k} + \gamma_k^* \beta_k^* &= 0.\end{aligned}\tag{S54}$$

It can be already deduced that  $\alpha_k = 0$  necessarily requires that  $|\gamma_k| = |\lambda_k|$ . This proof can also be applied to the case starting with the assumption that  $\beta_k = 0$ . Meanwhile, we would like to stress that  $|\gamma_k| = |\lambda_k|$  is not the sufficient condition to produce  $\alpha_k = 0$  or  $\beta_k = 0$ . This uncovers that the inversion winding numbers in Eq. (S52) are well protected by the spectral gap and the space-time inversion symmetry as long as  $|\lambda_k| \neq |\gamma_k|$ . Similar to the three-band case, this ill-defined condition  $|\lambda_k| = |\gamma_k|$  can be circumvented by adding some perturbations. As an example, we consider the following specific Bloch Hamiltonian:

$$H(k) = \begin{pmatrix} -\Delta & 0 & -\gamma & h_k \\ 0 & \Delta & g_k & -\gamma \\ -\gamma & g_k^* & \Delta & 0 \\ h_k^* & -\gamma & 0 & -\Delta \end{pmatrix},\tag{S55}$$

where  $h_k = -t_2 - t_1 e^{-ik}$ ,  $g_k = -t_1 - t_2 e^{ik}$ . Here,  $\gamma$  and  $t_{1,2}$  are respectively the inter-chain and intra-chain tunneling strengths,  $\pm\Delta$  is the on-site energy. The system has no chiral symmetry but preserves the inversion symmetry. In addition, the inversion winding numbers of gapped bands are always well-defined in this model.

Then, we tune the parameter and calculate the energy spectrum and the sublattice winding numbers, as shown in Fig. S7. It can be seen that there appear some in-gap states under OBC. In Fig. S7 (b-e), the inversion winding numbers only change their values at gap-closing points. Remarkably, it can be seen that the two inversion winding numbers  $(\nu_\alpha, \nu_\beta)$  are not exactly identical, which further provides a  $\mathbb{Z} \times \mathbb{Z}$  classification. As mentioned above, phase transitions among them are clearly accompanied by the gap closing to one of the nearest bands. Similarly, we also confirm that the polarization of each band is related to the sublattice winding number:  $p = \nu_{\alpha,\beta}/2 \pmod{1}$ . In addition, our approaches can be also applied to the chiral-symmetric case given that inversion symmetry is preserved. This example shows that, by studying the polarization between sublattices, we can find a

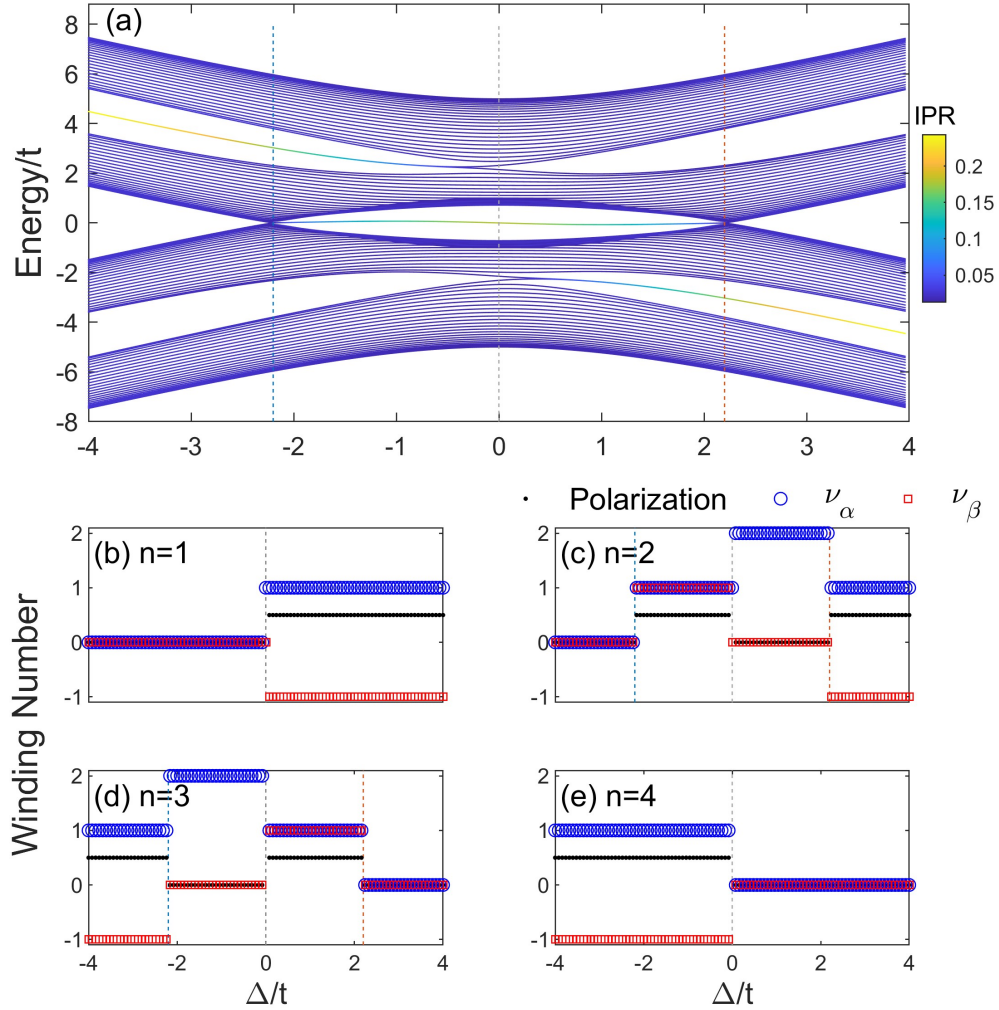


FIG. S7. Energy spectrum and winding number as a function of on-site energy. (a) Energy spectrum under OBC. The color of each point represents the IPR of each eigenstate. (b-e) Two sublattice winding numbers of the lowest ( $n = 1$ ) to the highest band ( $n = 4$ ). These winding numbers are computed under PBC through Eqs. (S52). In each plot, dashed lines indicate gap-closing points. Other parameters are chosen as:  $t_1 = 2$ ,  $t_2 = t = 1$  and  $\gamma = 2$ .

more fruitful classifications for the topological crystalline insulators.

---

[S1] L. Lin, Y. Ke, and C. Lee, Real-space representation of the winding number for a one-dimensional chiral-symmetric topological insulator, *Phys. Rev. B* **103**, 224208 (2021).

- [S2] L. Lin, Y. Ke, and C. Lee, Topological invariants for interacting systems: From twisted boundary conditions to center-of-mass momentum, *Phys. Rev. B* **107**, 125161 (2023).
- [S3] L. Lin, Y. Ke, L. Zhang, and C. Lee, Calculations of the chern number: Equivalence of real-space and twisted-boundary-condition formulas, *Phys. Rev. B* **108**, 174204 (2023).
- [S4] X.-L. Qi, Y.-S. Wu, and S.-C. Zhang, General theorem relating the bulk topological number to edge states in two-dimensional insulators, *Phys. Rev. B* **74**, 045125 (2006).
- [S5] L. Lin and C. Lee, Probing chiral-symmetric higher-order topological insulators with multipole winding number (2024), [arXiv:2401.03699 \[cond-mat.mes-hall\]](https://arxiv.org/abs/2401.03699).
- [S6] H. Watanabe, Insensitivity of bulk properties to the twisted boundary condition, *Phys. Rev. B* **98**, 155137 (2018).
- [S7] D. Wang, Y. Deng, J. Ji, M. Oudich, W. A. Benalcazar, G. Ma, and Y. Jing, Realization of a  $\mathbb{Z}$ -classified chiral-symmetric higher-order topological insulator in a coupling-inverted acoustic crystal, *Phys. Rev. Lett.* **131**, 157201 (2023).
- [S8] Y. Li, H. Qiu, Q. Zhang, and C. Qiu, Acoustic higher-order topological insulators protected by multipole chiral numbers, *Phys. Rev. B* **108**, 205135 (2023).